Hamiltonian discontinuous Galerkin FEM for linear, stratified (in)compressible Euler equations: internal gravity waves

Alexander M. van Oers [a],[*], Leo R.M. Maas [b],[a], Onno Bokhove [c]

[a] NIOZ Royal Netherlands Institute for Sea Research and Utrecht University, P.O. Box 59, 1790 AB Texel, The Netherlands
[b] Imau, Inst. for Marine and Atmospheric research Utrecht, Utrecht University, Princetonplein 5, 3584 CC, Utrecht, The Netherlands
[c] School of Mathematics, University of Leeds, LS2 9JT, Leeds, United Kingdom

A B S T R A C T

The linear equations governing internal gravity waves in a stratified ideal fluid possess a Hamiltonian structure. A discontinuous Galerkin finite element method has been developed in which this Hamiltonian structure is discretized, resulting in conservation of discrete analogs of phase space and energy. This required (i) the discretization of the Hamiltonian structure using alternating flux functions and symplectic time integration, (ii) the discretization of a divergence-free velocity field using Dirac's theory of constraints and (iii) the handling of large-scale computational demands due to the 3-dimensional nature of internal gravity waves and, in confined, symmetry-breaking fluid domains, possibly its narrow zones of attraction.

1. Introduction

In geophysical fluid dynamics internal gravity waves play an important role in the vertical transport of energy and momentum through the ocean. Internal gravity waves have their maximum displacement in the interior of a fluid. This is different from surface waves, which have their maximum displacement at the surface, or interfacial waves, which have their maximum displacement at the interface between two fluids. These internal gravity waves can only exist when the fluid in which they propagate is stratified in density, i.e. the density increases continuously in the direction of gravity. Fluid bodies in nature are often stably stratified in density due to differences in temperature or salt concentration. This provides these fluid bodies with a restoring force in terms of gravity that is absent in homogeneous fluids. This restoring force points in a particular direction, which renders the fluid anisotropic. Perturbations of such stably stratified fluids appear as waves that orient themselves to the anisotropic direction; they propagate under a particular fixed direction that is inclined with the anisotropy direction. Waves of given frequency (e.g. tides) preserve this inclination when reflecting from any boundary, also when reflecting from a sloping boundary. The consequence of this constraint is that for almost any shape of basin, these waves are focused onto a limit orbit, called a wave attractor [1,2]. The focusing on an attractor is accompanied by an intensification of the wave field, such that intense shearing motion is confined to the immediate vicinity of the wave attractor.

Wave attractors resulting from internal gravity waves have been numerically solved before. In [3–6] the equations of motion were discretized using well-established techniques. However, the equations governing internal gravity waves in an

---

ideal fluid possess a Hamiltonian structure, with a very distinct set of symmetry properties and conservation laws. These well-established discretization techniques do not take into account the underlying Hamiltonian structure of the equations. In [7] the importance of Hamiltonian dynamics in the construction of sophisticated numerical models for geophysical flows is underlined. In geophysical fluid dynamics there exist conserved quantities that are embedded in the equations of motion. Such quantities play a fundamental role in the description of the state and the dynamics of the system. By incorporating a discrete version of the conservation laws for these conserved quantities, we hope to see an improvement in the efficiency of our numerical models and to prevent spurious diffusive behavior. For example, in the case of Burgers equation, conservation of momentum is crucial to capture accurately the speed of any shocks that form [8]. In [9], Sadourny shows that conservation of energy and enstrophy is important for accurately capturing nonlinear transfers of energy to small scales. Each conservation law that is obeyed by the discrete system constrains the numerical solution. When both the numerical discretization and the differential equations obey analogs of the same conservation laws, the numerical solution behaves closer to the exact solution. The numerical solution will always have an error, but the error does not violate the enforced conservation laws.

Recently, the importance of Hamiltonian dynamics for the numerical approximations to wave attractors has been realized. As argued in [10], wave attractors are governed by linear equations, yet their behavior is reminiscent of a nonlinear system. Due to this nonlinear behavior, only few analytical statements can be made about wave attractors and only few analytical solutions are known [11]. We try to incorporate the analytical properties we do know about, like conservation of energy, to ensure our numerical simulations correctly capture the behavior of wave attractors. The focusing of internal waves onto limit cycles leads to the formation of small scales and to a build up of energy at the limit cycles. Hamiltonian techniques can ensure that energy is conserved and thus that energy build up at the attractor is correctly simulated. In [12] a finite difference method was developed for two-dimensional linear incompressible internal gravity waves with a uniform stratification. In [13] a discontinuous Galerkin finite element method was developed for three-dimensional linear (in)compressible inertial waves in a homogeneous, uniformly rotating, fluid. In both papers the Hamiltonian dynamics were identified and the equations were discretized such that the discrete system possessed discrete Hamiltonian dynamics. The preservation of the Hamiltonian structure ensured energy conservation.

We expand the work of [13] and [14] by applying their methodology to a new type of phenomenon, internal gravity waves. The stratification in background density forms a complicating factor. We show that the Hamiltonian dynamics can still be inherited by the discrete system, even in a three-dimensional domain and with non-uniform stratification. This required the incorporation of the background density in the construction of a discrete Poisson bracket.

A discontinuous Galerkin finite element method (DGFEM) has been chosen as numerical method since it allows for complex domain geometries, h-adaptivity (refinement of the mesh), p-adaptivity (refinement of the order of approximation) as well as r-adaptivity (movement of the nodes of the mesh) and is ideally suited for conservation laws. By discretizing the Hamiltonian structure of the compressible stratified Euler equations, phase space conservation and exact conservation of energy are ensured. Applying Dirac's method of constrained Hamiltonian dynamics [15–17] to the discretized compressible, stratified Euler equations enforce the incompressibility constraint and the velocity field stays divergence-free. This approach is preferable to discretizing the Hamiltonian structure for incompressible fluids directly since the discretization of the compressible Hamiltonian formulation is an intermediate check point. In addition, the Hamiltonian discretization of the compressible fluid equations and subsequent use of Dirac's theory appeared easier (to us) than discretizing the incompressible fluid equations directly in a Hamiltonian manner. By applying a symplectic time discretization the discrete Hamiltonian structure is conserved in time. The computational linear algebra demands are handled by using the Portable, Extensible Toolkit for Scientific Computation (PETSc) [18,19] in the DGFEM software environment hpGEM [20].

The outline of this paper is as follows. In Section 2, we review the equations of motion for stratified fluids, both for compressible and incompressible fluids, and their Hamiltonian formulations. In Section 3, we derive the Hamiltonian DGFEM for a compressible fluid and we use Dirac's theory to derive the Hamiltonian DGFEM for an incompressible fluid. In Section 4, we apply the modified midpoint rule, a symplectic time integrator, to our Hamiltonian DGFEM and discuss some of the properties of the resulting numerical schemes. In Section 5, we compare simulations with exact solutions of linear stratified fluids in closed and periodic, two- and three-dimensional domains. In Section 6, we draw our conclusions.

2. Continuum theory for stratified fluids

2.1. Governing equations

Internal gravity waves in a compressible inviscid fluid are governed by the Euler equations in primitive form:

$$
\begin{aligned}
\frac{\partial (\hat{\rho}\underline{\hat{v}})}{\partial t} &= -\hat{\rho}(\underline{\hat{v}} \cdot \nabla)\underline{\hat{v}} - \underline{\hat{v}}\nabla \cdot \left(\hat{\rho}\underline{\hat{v}}\right) - \nabla\hat{p} - g\hat{\rho}\underline{\hat{z}}, \\
\frac{\partial \hat{\rho}}{\partial t} &= -\nabla \cdot (\hat{\rho}\underline{\hat{v}}), \\
\frac{\partial \hat{p}}{\partial t} &= -\underline{\hat{v}} \cdot \nabla\hat{p} - c_s^2 \hat{\rho}\nabla \cdot \underline{\hat{v}},
\end{aligned}
\tag{1}
$$

where $\hat{\underline{v}} = \hat{\underline{v}}(x, y, z, t) = (\hat{u}, \hat{v}, \hat{w})^T$ is the three-dimensional velocity field, $\hat{\rho} = \hat{\rho}(x, y, z, t)$ the scalar density field, $\hat{p} = \hat{p}(x, y, z, t)$ the scalar pressure field, g the gravitational acceleration and $c_s^2 = (\partial p / \partial \rho)_s$ the speed of sound. The subscript s means taking the derivative while keeping the entropy s constant. Cartesian coordinates $\underline{x} = (x, y, z)$ and time t are used. The direction of gravity is aligned with the z-axis, indicated by the unit vector $\hat{\underline{z}}$. We denote the domain by Ω and the domain boundaries by $\partial\Omega$.

We linearize (1) around a hydrostatic background state. The background density $\rho_0(z)$ consists of a mean background density ρ^* and a varying background density $\bar{\rho}(z)$. We linearize such that $\hat{\underline{v}} = \underline{0} + \epsilon\underline{v}$, $\hat{\rho} = \rho_0(z) + \epsilon\rho$ and $\hat{p} = p_0(z) + \epsilon p$, where p_0 is the hydrostatic pressure related to ρ_0. The quantities $\underline{v}, \rho$ and p are perturbation quantities and ϵ is a small parameter. Linearization yields the compressible stratified Euler equations

$$\frac{\partial(\rho_0\underline{v})}{\partial t} = -\nabla p - \rho g\hat{\underline{z}},$$
$$\frac{\partial\rho}{\partial t} = -\nabla \cdot (\rho_0\underline{v}), \tag{2}$$
$$\frac{\partial p}{\partial t} = \rho_0 gw - c_0^2\rho_0\nabla \cdot \underline{v},$$

where $c_0^2 = c_0^2(z)$ is the linearized speed of sound and we employed hydrostatic balance in (2)-3. The strength of the background stratification is characterized by the buoyancy frequency or Brunt–Väisälä frequency,

$$N^2(z) = -\frac{g}{\rho_0}\frac{d\rho_0}{dz} - \frac{g^2}{c_0^2}. \tag{3}$$

For the stratification to be stable $N^2 > 0$, which says that denser liquid must lie below liquid of lesser density (and that the rate of change of background density with depth is larger than the adiabatic lapse rate, g/c_0^2).

Taking the limit of zero Mach number, $\mathrm{Ma} = U/c$, with U a constant reference velocity and c a constant reference speed of sound for the fluid, the incompressible stratified Euler equations arise from (2) as

$$\frac{\partial(\rho_0\underline{v})}{\partial t} = -\nabla P - \rho g\hat{\underline{z}},$$
$$\frac{\partial\rho}{\partial t} = -w\frac{d\rho_0}{dz}, \quad \nabla \cdot \underline{v} = 0. \tag{4}$$

The pressure is no longer a thermodynamic variable but an arbitrary function that ensures the velocity field is divergence-free; hence the pressure is now denoted by P. The destabilizing, second term in the definition of the buoyancy frequency, (3), disappears in the limit of zero Mach number.

When the varying part of the background density, $\bar{\rho}(z)$, is much less than the constant part of the background density, ρ^*, the Boussinesq approximation is made. In the Boussinesq approximation the varying part of the background density is neglected in the inertia terms and in the denominator of the buoyancy frequency:

$$\frac{\partial(\rho^*\underline{v})}{\partial t} = -\nabla P - \rho g\hat{\underline{z}},$$
$$\frac{\partial\rho}{\partial t} = \frac{N^2}{g}\rho^* w, \quad \nabla \cdot \underline{v} = 0, \tag{5}$$

with buoyancy frequency

$$N^2(z) = -\frac{g}{\rho^*}\frac{d\rho_0}{dz}. \tag{6}$$

Two types of boundary conditions are used for systems (2), (4) and (5): periodic or solid wall boundary conditions. In the inviscid case, for the solid wall boundary conditions the velocity normal to the boundary has to vanish, $\hat{\underline{n}} \cdot \underline{v} = 0$, where $\hat{\underline{n}}$ is the outward normal.

2.2. Hamiltonian framework

Hamiltonian dynamics describe the evolution of conservative physical systems. In general, a Hamiltonian system consists of a phase space and two geometric objects, an energy functional $\mathcal{H}$ and a Poisson bracket $\{\cdot, \cdot\}$ [21,22]. The Hamiltonian dynamics is given by the time evolution of a general state functional $\mathcal{F}$ via the bracket form

$$\frac{d\mathcal{F}}{dt} = \{\mathcal{F}, \mathcal{H}\}. \tag{7}$$

The Poisson bracket $\{\mathcal{F}, \mathcal{H}\}$ has to satisfy

- skew-symmetry: $\{\mathcal{F}, \mathcal{H}\} = -\{\mathcal{H}, \mathcal{F}\}$,
- linearity: $\{\alpha\mathcal{F} + \beta\mathcal{G}, \mathcal{H}\} = \alpha\{\mathcal{F}, \mathcal{H}\} + \beta\{\mathcal{G}, \mathcal{H}\}$,
- Jacobi identity: $\{\mathcal{F}, \{\mathcal{G}, \mathcal{H}\}\} + \{\mathcal{G}, \{\mathcal{H}, \mathcal{F}\}\} + \{\mathcal{H}, \{\mathcal{F}, \mathcal{G}\}\} = 0$,
- Leibniz rule: $\{\mathcal{F}\mathcal{G}, \mathcal{H}\} = \mathcal{F}\{\mathcal{G}, \mathcal{H}\} + \{\mathcal{F}, \mathcal{H}\}\mathcal{G}$,

where α and β are constants and $\mathcal{F}, \mathcal{G}$ and $\mathcal{H}$ are functionals.

For a function $u(\underline{x}, t)$ in a domain Ω, with $(x, y, z) = \underline{x} \in \Omega$ and time t, a functional $\mathcal{F}[u(\cdot)]$ maps real-valued functions $u(\underline{x}, t)$ into real numbers [23]. Then $\delta\mathcal{F}/\delta u$, the functional derivative of $\mathcal{F}$ with respect to u, is defined to be that function of $\underline{x}$ and t for which the change in $\mathcal{F}$ due to a small variation $\epsilon\delta u$ in the function u is given by [22]

$$\delta\mathcal{F} = \lim_{\epsilon \to 0} \frac{\mathcal{F}[u + \epsilon\delta u] - \mathcal{F}[u]}{\epsilon} = \frac{d}{d\epsilon}\mathcal{F}[u + \epsilon\delta u]\Big|_{\epsilon=0} = \int_{\Omega} \frac{\delta\mathcal{F}}{\delta u}\delta u(\underline{x}, t)\,d\underline{x}. \tag{8}$$

2.3. Poisson bracket for linearized compressible fluid

The Hamiltonian dynamics corresponding to (1) in $\Omega \subset \mathbb{R}^3$ is found in [24,25] after a transformation of variables. The Hamiltonian dynamics corresponding to (2) is found by adapting the Poisson bracket for the linear equations [26,27]:

$$\begin{aligned}
\frac{d\mathcal{F}}{dt} = \{\mathcal{F}, \mathcal{H}\} = &\int_{\Omega} \frac{\delta\mathcal{H}}{\delta\rho}\nabla\cdot\left(\rho_0\frac{\delta\mathcal{F}}{\delta(\rho_0\underline{v})}\right) - \frac{\delta\mathcal{F}}{\delta\rho}\nabla\cdot\left(\rho_0\frac{\delta\mathcal{H}}{\delta(\rho_0\underline{v})}\right) \\
&+ \frac{\delta\mathcal{F}}{\delta p}\left(\rho_0 g\frac{\delta\mathcal{H}}{\delta(\rho_0 w)} - c_0^2\rho_0\nabla\cdot\frac{\delta\mathcal{H}}{\delta(\rho_0\underline{v})}\right) - \frac{\delta\mathcal{H}}{\delta p}\left(\rho_0 g\frac{\delta\mathcal{F}}{\delta(\rho_0 w)} - c_0^2\rho_0\nabla\cdot\frac{\delta\mathcal{F}}{\delta(\rho_0\underline{v})}\right)\,d\underline{x}
\end{aligned} \tag{9}$$

with Hamiltonian [27,28]

$$\mathcal{H} = \int_{\Omega} \frac{1}{2}\rho_0|\underline{v}|^2 + \frac{1}{2}\frac{g^2}{\rho_0 N^2}\left(\rho - \frac{p}{c_0^2}\right)^2 + \frac{1}{2}\frac{p^2}{\rho_0 c_0^2}\,d\underline{x}. \tag{10}$$

Functional derivatives of $\mathcal{H}$ follow from (8) as

$$\delta\mathcal{H} = \int_{\Omega} \frac{\delta\mathcal{H}}{\delta(\rho_0\underline{v})}\cdot\delta(\rho_0\underline{v}) + \frac{\delta\mathcal{H}}{\delta\rho}\delta\rho + \frac{\delta\mathcal{H}}{\delta p}\delta p\,d\underline{x} \tag{11}$$

and are

$$\frac{\delta\mathcal{H}}{\delta(\rho_0\underline{v})} = \underline{v}, \quad \frac{\delta\mathcal{H}}{\delta\rho} = \frac{g^2}{\rho_0 N^2}\left(\rho - \frac{p}{c_0^2}\right), \quad \frac{\delta\mathcal{H}}{\delta p} = \frac{g^2}{\rho_0 N^2}\left(\frac{p}{c_0^4} - \frac{\rho}{c_0^2}\right) + \frac{p}{\rho_0 c_0^2}. \tag{12}$$

To obtain (2), we first substitute these variations into the Poisson bracket (9),

$$\begin{aligned}
&\frac{d\mathcal{F}}{dt} = \{\mathcal{F}, \mathcal{H}\} = \\
&\int_{\Omega} \frac{g^2}{\rho_0 N^2}\left(\rho - \frac{p}{c_0^2}\right)\nabla\cdot\left(\rho_0\frac{\delta\mathcal{F}}{\delta(\rho_0\underline{v})}\right) - \frac{\delta\mathcal{F}}{\delta\rho}\nabla\cdot(\rho_0\underline{v}) + \frac{\delta\mathcal{F}}{\delta p}\left(\rho_0 g w - c_0^2\rho_0\nabla\cdot\underline{v}\right) \\
&- \left(\frac{g^2}{\rho_0 N^2}\left(\frac{p}{c_0^4} - \frac{\rho}{c_0^2}\right) + \frac{p}{\rho_0 c_0^2}\right)\left(\rho_0 g\frac{\delta\mathcal{F}}{\delta(\rho_0 w)} - c_0^2\rho_0\nabla\cdot\frac{\delta\mathcal{F}}{\delta(\rho_0\underline{v})}\right)\,d\underline{x}.
\end{aligned} \tag{13}$$

Then we choose functionals as [13]

$$\mathcal{F}_\rho = \int_{\Omega} \rho(\underline{x}, t)\phi_\rho(\underline{x})\,d\underline{x}, \quad \mathcal{F}_p = \int_{\Omega} p(\underline{x}, t)\phi_p(\underline{x})\,d\underline{x}, \quad \mathcal{F}_{\rho_0\underline{v}} = \int_{\Omega} (\rho_0\underline{v})(\underline{x}, t)\cdot\underline{\phi}_{\rho_0\underline{v}}(\underline{x})\,d\underline{x}, \tag{14}$$

with $\phi_\rho, \phi_p \in \mathcal{V}$ and $\underline{\phi}_{\rho_0\underline{v}} \in \mathcal{W}$ arbitrary test functions, where

$$\mathcal{V} = \left\{\phi \in L^2(\Omega)\right\}, \quad \mathcal{W} = \left\{\underline{\phi} \in \left(L^2(\Omega)\right)^3 : \nabla\cdot\underline{\phi} \in L^2(\Omega) \text{ and } \hat{\underline{n}}\cdot\underline{\phi} = 0 \text{ at } \partial\Omega\right\} \tag{15}$$

and $L^2(\Omega)$ is the space of square integrable functions on Ω. The space of restricted test functions, $\mathcal{W}$, ensures the satisfaction of the solid wall boundary condition. The functional derivatives of (14) are

$$\frac{\delta\mathcal{F}_\rho}{\delta\rho} = \phi_\rho(\underline{x}), \quad \frac{\delta\mathcal{F}_p}{\delta p} = \phi_p(\underline{x}), \quad \frac{\delta\mathcal{F}_{\rho_0\underline{v}}}{\delta(\rho_0\underline{v})} = \underline{\phi}_{\rho_0\underline{v}}(\underline{x}), \text{ with } \frac{\delta\mathcal{F}_{\rho_0\underline{v}}}{\delta(\rho_0\underline{v})} \cdot \hat{\underline{n}} = 0 \text{ at } \partial\Omega. \tag{16}$$

Using these functionals in (13) and the arbitrariness of the test functions yields (2). To evaluate the momentum equations, we split the contributions in the horizontal directions, denoted by the subscript H, and the vertical direction. The momentum equations obtained from the bracket are

$$\frac{\partial(\rho_0\underline{v}_H)}{\partial t} = -\rho_0\nabla_H\left[\frac{g^2}{\rho_0 N^2}\left(\rho - \frac{p}{c_0^2}\right)\right] - \nabla_H\left[c_0^2\rho_0\left(\frac{g^2}{\rho_0 N^2}\left(\frac{p}{c_0^4} - \frac{\rho}{c_0^2}\right) + \frac{p}{\rho_0 c_0^2}\right)\right],$$

$$\frac{\partial(\rho_0 w)}{\partial t} = -\rho_0\frac{\partial}{\partial z}\left[\frac{g^2}{\rho_0 N^2}\left(\rho - \frac{p}{c_0^2}\right)\right] - \frac{\partial}{\partial z}\left[c_0^2\rho_0\left(\frac{g^2}{\rho_0 N^2}\left(\frac{p}{c_0^4} - \frac{\rho}{c_0^2}\right) + \frac{p}{\rho_0 c_0^2}\right)\right] \tag{17}$$

$$- \rho_0 g\left[\frac{g^2}{\rho_0 N^2}\left(\frac{p}{c_0^4} - \frac{\rho}{c_0^2}\right) + \frac{p}{\rho_0 c_0^2}\right],$$

where ∇_H is the gradient acting in the horizontal directions. Since the background density only varies in the vertical direction, the horizontal gradient does not act on the background density. Using $g^2 d\rho_0/dz/(\rho_0 N^2) = -g - g^3/(c_0^2 N^2)$ in (17)-2 yields (2)-1.

3. Discrete Hamiltonian formulation

In this section, we introduce a discontinuous Galerkin FEM discretization that preserves the Hamiltonian structure of the linear, compressible and incompressible fluids.

3.1. Finite element space

The physical domain Ω is approximated by a computational domain Ω_h, consisting of nonoverlapping elements K. The set of all edges of the computational domain is Γ, with Γ_i the set of interior edges. Let $e \in \Gamma_i$ be a face between a "left" element, K_L, and a "right" element, K_R, with corresponding outward normals $\hat{\underline{n}}_L$ and $\hat{\underline{n}}_R$. When f is a continuous function on K_L and K_R, but possibly discontinuous across the face e, let $f^L = (f|_{K_L})|_e$ and $f^R = (f|_{K_R})|_e$. Let $\mathcal{P}^{N_p}(K)$ be the space of polynomials of at most degree N_p on K. The finite element spaces required are

$$V_h = \left\{\psi \in L^2(\Omega) : \psi|_K \in \mathcal{P}^{N_p}(K), \forall K \in \Omega_h\right\},$$

$$W_h = \left\{\underline{\psi} \in \left(L^2(\Omega)\right)^3 : \underline{\psi}\big|_K \in \left(\mathcal{P}^{N_p}(K)\right)^3, \forall K \in \Omega_h \text{ and } \hat{\underline{n}} \cdot \underline{\psi}\big|_{\partial\Omega} = 0\right\}, \tag{18}$$

where $L^2(\Omega)$ is the space of square integrable functions on Ω. The specific functional $F[(\rho_0\underline{v})_h] = \int_\Omega (\rho_0\underline{v})_h \cdot \underline{\psi} \, d\underline{x}$ is chosen to obtain the discretized momentum equations in a Hamiltonian framework, with $\underline{\psi} \in W_h$ an arbitrary test function. The functional derivative with respect to the momentum equals

$$\frac{\delta F}{\delta(\rho_0\underline{v})_h} = \underline{\psi}. \tag{19}$$

Likewise, functionals $F[\rho_h] = \int_\Omega \rho_h\psi \, d\underline{x}$ and $F[p_h] = \int_\Omega p_h\psi \, d\underline{x}$, with $\psi \in V_h$, are needed [13].

The equations (2) and corresponding Poisson bracket (9) and Hamiltonian (10) are scaled such that we introduce the Mach number and we can take $g = c_0^2 = 1$. We assume that the speed of sound is constant. The discrete Hamiltonian is

$$H = \sum_{K \in \Omega_h}\int_K \frac{1}{2}\frac{1}{\rho_0}\left(\rho_0\underline{v}\right)_h^2 + \frac{1}{2}\frac{1}{\rho_0 N^2}\left(\rho_h - \mathrm{Ma}^2 p_h\right)^2 + \frac{1}{2}\frac{\mathrm{Ma}^2 p_h^2}{\rho_0} \, dK, \tag{20}$$

where $\left(\rho_0\underline{v}\right)_h \in W_h$ and $\rho_h, p_h \in V_h$ are the discrete variables. The parameters ρ_0, $d\rho_0/dz$ and N^2 are taken in the same function space V_h. The variational derivatives are

$$\frac{\delta H}{\delta(\rho_0\underline{v})_h} = \underline{v}_h, \qquad \frac{\delta H}{\delta\rho_h} = \frac{1}{\rho_0 N^2}\left(\rho_h - \mathrm{Ma}^2 p_h\right),$$

$$\frac{\delta H}{\delta p_h} = \frac{1}{\rho_0 N^2}\left(\mathrm{Ma}^4 p_h - \mathrm{Ma}^2 \rho_h\right) + \frac{\mathrm{Ma}^2 p_h}{\rho_0}. \tag{21}$$

There is some abuse of notation here, because the functions F and H are used for functionals. However, if approximations $(\rho_0 \underline{v})_h$, ρ_h and p_h are viewed as finite-dimensional expansions, then function derivatives with respect to the expansion coefficients emerge.

3.2. Hamiltonian DGFEM discretization for linearized compressible stratified fluid

We limit the functionals in the Poisson bracket (9) to ones on the approximate finite element space to arrive at an interim discrete Poisson bracket,

$$
\begin{aligned}
[F, G] = \sum_{K \in \Omega_h} \int_K \frac{\delta G}{\delta \rho_h} \nabla_h \cdot \left(\rho_0 \frac{\delta F}{\delta (\rho_0 \underline{v})_h} \right) - \frac{\delta F}{\delta \rho_h} \nabla_h \cdot \left(\rho_0 \frac{\delta G}{\delta (\rho_0 \underline{v})_h} \right) \\
+ \frac{\delta F}{\delta p_h} \left(\rho_0 \frac{\delta G}{\delta (\rho_0 w)_h} - \frac{\rho_0}{\mathrm{Ma}^2} \nabla_h \cdot \left(\frac{\delta G}{\delta (\rho_0 \underline{v})_h} \right) \right) \\
- \frac{\delta G}{\delta p_h} \left(\rho_0 \frac{\delta F}{\delta (\rho_0 w)_h} - \frac{\rho_0}{\mathrm{Ma}^2} \nabla_h \cdot \left(\frac{\delta F}{\delta (\rho_0 \underline{v})_h} \right) \right) \, dK,
\end{aligned}
\tag{22}
$$

with element-wise differential operator ∇_h. This interim bracket is incomplete because there is no connection between the elements, an issue that is repaired next. Working out the terms involving density variations and integrating by parts allows the introduction of numerical fluxes into the Poisson bracket,

$$
\begin{aligned}
[F, G] = & \sum_{K \in \Omega_h} \int_K -\nabla_h \left(\rho_0 \frac{\delta G}{\delta \rho_h} \right) \cdot \frac{\delta F}{\delta (\rho_0 \underline{v})_h} + \nabla_h \left(\rho_0 \frac{\delta F}{\delta \rho_h} \right) \cdot \frac{\delta G}{\delta (\rho_0 \underline{v})_h} \, dK \\
& + \sum_{K \in \Omega_h} \int_{\partial K} \rho_0 \frac{\delta G}{\delta \rho_h} \hat{\underline{n}} \cdot \widehat{\frac{\delta F}{\delta (\rho_0 \underline{v})_h}} - \widehat{\frac{\delta G}{\delta (\rho_0 \underline{v})_h}} \cdot \hat{\underline{n}} \rho_0 \frac{\delta F}{\delta \rho_h} \, d\Gamma \\
& + \sum_{K \in \Omega_h} \int_K \frac{d\rho_0}{dz} \left(\frac{\delta G}{\delta \rho_h} \frac{\delta F}{\delta (\rho_0 w)_h} - \frac{\delta F}{\delta \rho_h} \frac{\delta G}{\delta (\rho_0 w)_h} \right) dK \\
& - \sum_{K \in \Omega_h} \int_K \rho_0 \left(\frac{\delta G}{\delta p_h} \frac{\delta F}{\delta (\rho_0 w)_h} - \frac{\delta F}{\delta p_h} \frac{\delta G}{\delta (\rho_0 w)_h} \right) dK \\
& + \frac{1}{\mathrm{Ma}^2} \sum_{K \in \Omega_h} \int_K -\nabla_h \left(\rho_0 \frac{\delta G}{\delta p_h} \right) \cdot \frac{\delta F}{\delta (\rho_0 \underline{v})_h} + \nabla_h \left(\rho_0 \frac{\delta F}{\delta p_h} \right) \cdot \frac{\delta G}{\delta (\rho_0 \underline{v})_h} \, dK \\
& + \frac{1}{\mathrm{Ma}^2} \sum_{K \in \Omega_h} \int_{\partial K} \rho_0 \frac{\delta G}{\delta p_h} \hat{\underline{n}} \cdot \widehat{\frac{\delta F}{\delta (\rho_0 \underline{v})_h}} - \widehat{\frac{\delta G}{\delta (\rho_0 \underline{v})_h}} \cdot \hat{\underline{n}} \rho_0 \frac{\delta F}{\delta p_h} \, d\Gamma,
\end{aligned}
\tag{23}
$$

where wide hats indicate numerical fluxes. Remarkable about this discretization is that the numerical fluxes also work on the test functions. When choosing the numerical flux $\widehat{\frac{\delta F}{\delta (\rho_0 \underline{v})_h}}$ the same as for $\widehat{\frac{\delta G}{\delta (\rho_0 \underline{v})_h}}$, the discrete bracket is skew-symmetric. We choose the following alternating fluxes

$$
\widehat{\frac{\delta F}{\delta (\rho_0 \underline{v})_h}} = (1 - \theta) \frac{\delta F}{\delta (\rho_0 \underline{v})_h^L} + \theta \frac{\delta F}{\delta (\rho_0 \underline{v})_h^R}, \qquad \widehat{\frac{\delta G}{\delta (\rho_0 \underline{v})_h}} = (1 - \theta) \frac{\delta G}{\delta (\rho_0 \underline{v})_h^L} + \theta \frac{\delta G}{\delta (\rho_0 \underline{v})_h^R},
\tag{24}
$$

where the superscript L indicates the element to the left of the boundary and the superscript R indicates the element to the right of the boundary. The parameter $0 \le \theta \le 1$ controls the type of flux function.

Substituting expressions (24) for the numerical fluxes in (23) and rewriting the summation over all elements for the boundary fluxes into a summation over all interior boundaries yields

$$
\begin{aligned}
[F, G] =\ & \sum_K \int_K -\nabla_h \left(\frac{\delta G}{\delta \rho_h} \rho_0 \right) \cdot \frac{\delta F}{\delta (\rho_0 \underline{v})_h} + \nabla_h \left(\frac{\delta F}{\delta \rho_h} \rho_0 \right) \cdot \frac{\delta G}{\delta (\rho_0 \underline{v})_h}\, \mathrm{d}K \\
& + \sum_{e \in \Gamma_i} \int_e \left(\rho_0^L \frac{\delta G}{\delta \rho_h^L} - \rho_0^R \frac{\delta G}{\delta \rho_h^R} \right) \hat{\underline{n}}^L \cdot \left((1-\theta) \frac{\delta F}{\delta (\rho_0 \underline{v})_h^L} + \theta \frac{\delta F}{\delta (\rho_0 \underline{v})_h^R} \right) \\
& \qquad - \left(\rho_0^L \frac{\delta F}{\delta \rho_h^L} - \rho_0^R \frac{\delta F}{\delta \rho_h^R} \right) \hat{\underline{n}}^L \cdot \left((1-\theta) \frac{\delta G}{\delta (\rho_0 \underline{v})_h^L} + \theta \frac{\delta G}{\delta (\rho_0 \underline{v})_h^R} \right) \mathrm{d}\Gamma \\
& + \sum_K \int_K \frac{\mathrm{d}\rho_0}{\mathrm{d}z} \left(\frac{\delta G}{\delta \rho_h} \frac{\delta F}{\delta (\rho_0 w)_h} - \frac{\delta F}{\delta \rho_h} \frac{\delta G}{\delta (\rho_0 w)_h} \right) \mathrm{d}K \\
& - \sum_K \int_K \rho_0 \left(\frac{\delta G}{\delta p_h} \frac{\delta F}{\delta (\rho_0 w)_h} - \frac{\delta F}{\delta p_h} \frac{\delta G}{\delta (\rho_0 w)_h} \right) \mathrm{d}K \\
& + \frac{1}{\mathrm{Ma}^2} \sum_K \int_K -\nabla_h \left(\rho_0 \frac{\delta G}{\delta p_h} \right) \cdot \frac{\delta F}{\delta (\rho_0 \underline{v})_h} + \nabla_h \left(\rho_0 \frac{\delta F}{\delta p_h} \right) \cdot \frac{\delta G}{\delta (\rho_0 \underline{v})_h}\, \mathrm{d}K \\
& + \frac{1}{\mathrm{Ma}^2} \sum_{e \in \Gamma_i} \int_e \left(\rho_0^L \frac{\delta G}{\delta p_h^L} - \rho_0^R \frac{\delta G}{\delta p_h^R} \right) \hat{\underline{n}}^L \cdot \left((1-\theta) \frac{\delta F}{\delta (\rho_0 \underline{v})_h^L} + \theta \frac{\delta F}{\delta (\rho_0 \underline{v})_h^R} \right) \\
& \qquad - \left(\rho_0^L \frac{\delta F}{\delta p_h^L} - \rho_0^R \frac{\delta F}{\delta p_h^R} \right) \hat{\underline{n}}^L \cdot \left((1-\theta) \frac{\delta G}{\delta (\rho_0 \underline{v})_h^L} + \theta \frac{\delta G}{\delta (\rho_0 \underline{v})_h^R} \right) \mathrm{d}\Gamma,
\end{aligned}
\tag{25}
$$

where $\hat{\underline{n}}^L$ is the exterior normal vector connected with element K_L. All numerical fluxes across the exterior boundaries are zero due to the periodic or solid wall boundary conditions. In a periodic domain, no exterior boundaries are present, so there is no numerical flux at the exterior boundaries. In a domain with solid walls, the boundary condition of no normal flow across a boundary is $\hat{\underline{n}} \cdot \underline{v} = 0$ at $\partial\Omega$. The same should hold for the corresponding numerical flux in the numerical domain. From (21) it follows

$$
\hat{\underline{n}} . \widehat{\frac{\delta H}{\delta (\rho_0 \underline{v})_h}} = 0 \quad \text{at} \quad \partial\Omega_h.
\tag{26}
$$

To ensure the skew-symmetry of the bracket a similar boundary condition is required for the arbitrary functions F

$$
\hat{\underline{n}} . \widehat{\frac{\delta F}{\delta (\rho_0 \underline{v})_h}} = 0 \quad \text{at} \quad \partial\Omega_h,
\tag{27}
$$

conform (15).

On each element the numerical solution is expanded using local basis functions,

$$
(\rho_0 \underline{v})_h^K (\underline{x}, t) = \sum_{\beta=1}^{N_p} (\rho_0 \underline{v})_\beta^K (t) \phi_\beta^K (\underline{x}), \qquad \rho_h^K (\underline{x}, t) = \sum_{\beta=1}^{N_p} \rho_\beta^K (t) \phi_\beta^K (\underline{x}), \qquad p_h^K (\underline{x}, t) = \sum_{\beta=1}^{N_p} p_\beta^K (t) \phi_\beta^K (\underline{x}),
\tag{28}
$$

where $(\rho_0 \underline{v})_\beta^K (t)$, etc. are the expansion coefficients. Dropping the superscript K again and using the summation convention simplifies the notation. Variational and function derivatives can now be related by [13,14]

$$
\begin{aligned}
\delta F =\ & \sum_K \int_K \frac{\delta F}{\delta (\rho_0 \underline{v})_h} \delta (\rho_0 \underline{v})_h + \frac{\delta F}{\delta \rho_h} \delta \rho_h + \frac{\delta F}{\delta p_h} \delta p_h\, \mathrm{d}K \\
=\ & \sum_K \int_K \frac{\delta F}{\delta (\rho_0 \underline{v})_h} \delta (\phi_\beta(\underline{x})(\rho_0 \underline{v})_\beta(t)) + \frac{\delta F}{\delta \rho_h} \delta (\phi_\beta(\underline{x}) \rho_\beta(t)) + \frac{\delta F}{\delta p_h} \delta (\phi_\beta(\underline{x}) p_\beta(t))\, \mathrm{d}K \\
=\ & \sum_K \left(\int_K \frac{\delta F}{\delta (\rho_0 \underline{v})_h} \phi_\beta(\underline{x})\, \mathrm{d}K \right) \delta (\rho_0 \underline{v})_\beta(t) + \left(\int_K \frac{\delta F}{\delta \rho_h} \phi_\beta(\underline{x})\, \mathrm{d}K \right) \delta \rho_\beta(t) + \left(\int_K \frac{\delta F}{\delta p_h} \phi_\beta(\underline{x})\, \mathrm{d}K \right) \delta p_\beta(t) \\
=\ & \sum_K \frac{\partial F}{\partial (\rho_0 \underline{v})_\beta} \delta (\rho_0 \underline{v})_\beta(t) + \frac{\partial F}{\partial \rho_\beta} \delta \rho_\beta(t) + \frac{\partial F}{\partial p_\beta} \delta p_\beta(t).
\end{aligned}
\tag{29}
$$

We define the local mass matrix $M_{\alpha\beta}^K = M_{\alpha\beta}$ as

$$M_{\alpha\beta} = \int\limits_K \phi_\alpha \phi_\beta \, dK, \tag{30}$$

then, using (28)-1, the following holds

$$M_{\alpha\beta} \left(\rho_0 \underline{v} \right)_\beta = \int\limits_K \phi_\alpha \left(\rho_0 \underline{v} \right)_h \, dK. \tag{31}$$

From (29), it follows that

$$\frac{\delta F}{\delta (\rho_0 \underline{v})_h} = M_{\beta\gamma}^{-1} \frac{\partial F}{\partial (\rho_0 \underline{v})_\beta} \phi_\gamma, \quad \frac{\delta F}{\delta \rho_h} = M_{\beta\gamma}^{-1} \frac{\partial F}{\partial \rho_\beta} \phi_\gamma, \quad \frac{\delta F}{\delta p_h} = M_{\beta\gamma}^{-1} \frac{\partial F}{\partial p_\beta} \phi_\gamma. \tag{32}$$

Substituting these relations into (25) yields the finite-dimensional Poisson bracket

$$
\begin{aligned}
[F, G] = &\sum_K \left(\frac{\partial G}{\partial (\rho_0 \underline{v})_\beta} \frac{\partial F}{\partial \rho_\alpha} - \frac{\partial F}{\partial (\rho_0 \underline{v})_\beta} \frac{\partial G}{\partial \rho_\alpha} \right) \cdot \underline{E}_{\gamma\mu} M_{\alpha\mu}^{-1} M_{\beta\gamma}^{-1} \\
&+ \left(\frac{\partial G}{\partial (\rho_0 w)_\beta} \frac{\partial F}{\partial p_\alpha} - \frac{\partial F}{\partial (\rho_0 w)_\beta} \frac{\partial G}{\partial p_\alpha} \right) N_{\gamma\mu} M_{\alpha\mu}^{-1} M_{\beta\gamma}^{-1} \\
&- \left(\frac{\partial G}{\partial (\rho_0 w)_\beta} \frac{\partial F}{\partial \rho_\alpha} - \frac{\partial F}{\partial (\rho_0 w)_\beta} \frac{\partial G}{\partial \rho_\alpha} \right) \check{N}_{\gamma\mu} M_{\alpha\mu}^{-1} M_{\beta\gamma}^{-1} \\
&+ \frac{1}{\mathrm{Ma}^2} \left(\frac{\partial G}{\partial (\rho_0 \underline{v})_\beta} \frac{\partial F}{\partial p_\alpha} - \frac{\partial F}{\partial (\rho_0 \underline{v})_\beta} \frac{\partial G}{\partial p_\alpha} \right) \cdot \underline{E}_{\gamma\mu} M_{\alpha\mu}^{-1} M_{\beta\gamma}^{-1} \\
&+ \sum_{e \in \Gamma_i} \left(\frac{\partial G}{\partial \rho_\alpha^L} \frac{\partial F}{\partial (\rho_0 \underline{v})_\beta^L} - \frac{\partial F}{\partial \rho_\alpha^L} \frac{\partial G}{\partial (\rho_0 \underline{v})_\beta^L} \right) \cdot (1 - \theta) \underline{G}_{\gamma\mu}^{LL} M_{\alpha\mu}^{-L} M_{\beta\gamma}^{-L} \\
&+ \left(\frac{\partial G}{\partial \rho_\alpha^L} \frac{\partial F}{\partial (\rho_0 \underline{v})_\beta^R} - \frac{\partial F}{\partial \rho_\alpha^L} \frac{\partial G}{\partial (\rho_0 \underline{v})_\beta^R} \right) \cdot \theta \underline{G}_{\gamma\mu}^{RL} M_{\alpha\mu}^{-L} M_{\beta\gamma}^{-R} \\
&- \left(\frac{\partial G}{\partial \rho_\alpha^R} \frac{\partial F}{\partial (\rho_0 \underline{v})_\beta^L} - \frac{\partial F}{\partial \rho_\alpha^R} \frac{\partial G}{\partial (\rho_0 \underline{v})_\beta^L} \right) \cdot (1 - \theta) \underline{G}_{\gamma\mu}^{LR} M_{\alpha\mu}^{-R} M_{\beta\gamma}^{-L} \\
&- \left(\frac{\partial G}{\partial \rho_\alpha^R} \frac{\partial F}{\partial (\rho_0 \underline{v})_\beta^R} - \frac{\partial F}{\partial \rho_\alpha^R} \frac{\partial G}{\partial (\rho_0 \underline{v})_\beta^R} \right) \cdot \theta \underline{G}_{\gamma\mu}^{RR} M_{\alpha\mu}^{-R} M_{\beta\gamma}^{-R} \\
&+ \frac{1}{\mathrm{Ma}^2} \left(\frac{\partial G}{\partial p_\alpha^L} \frac{\partial F}{\partial (\rho_0 \underline{v})_\beta^L} - \frac{\partial F}{\partial p_\alpha^L} \frac{\partial G}{\partial (\rho_0 \underline{v})_\beta^L} \right) \cdot (1 - \theta) \underline{G}_{\gamma\mu}^{LL} M_{\alpha\mu}^{-L} M_{\beta\gamma}^{-L} \\
&+ \frac{1}{\mathrm{Ma}^2} \left(\frac{\partial G}{\partial p_\alpha^L} \frac{\partial F}{\partial (\rho_0 \underline{v})_\beta^R} - \frac{\partial F}{\partial p_\alpha^L} \frac{\partial G}{\partial (\rho_0 \underline{v})_\beta^R} \right) \cdot \theta \underline{G}_{\gamma\mu}^{RL} M_{\alpha\mu}^{-L} M_{\beta\gamma}^{-R} \\
&- \frac{1}{\mathrm{Ma}^2} \left(\frac{\partial G}{\partial p_\alpha^R} \frac{\partial F}{\partial (\rho_0 \underline{v})_\beta^L} - \frac{\partial F}{\partial p_\alpha^R} \frac{\partial G}{\partial (\rho_0 \underline{v})_\beta^L} \right) \cdot (1 - \theta) \underline{G}_{\gamma\mu}^{LR} M_{\alpha\mu}^{-R} M_{\beta\gamma}^{-L} \\
&- \frac{1}{\mathrm{Ma}^2} \left(\frac{\partial G}{\partial p_\alpha^R} \frac{\partial F}{\partial (\rho_0 \underline{v})_\beta^R} - \frac{\partial F}{\partial p_\alpha^R} \frac{\partial G}{\partial (\rho_0 \underline{v})_\beta^R} \right) \cdot \theta \underline{G}_{\gamma\mu}^{RR} M_{\alpha\mu}^{-R} M_{\beta\gamma}^{-R}
\end{aligned}
\tag{33}
$$

with elemental (vector) matrices

$$\underline{E}_{\gamma\mu} = \int\limits_K \phi_\gamma \nabla_h \left(\rho_0 \phi_\mu \right) \, dK \qquad \text{and} \qquad \underline{G}_{\gamma\mu}^{RL} = \int\limits_e \underline{\hat{n}}^L \phi_\gamma^R \rho_0^L \phi_\mu^L \, d\Gamma, \tag{34}$$

and similar relations for the other boundary terms, and matrices

$$N_{\gamma\mu} = \int\limits_K \phi_\gamma \rho_0 \phi_\mu \, dK \qquad \text{and} \qquad \check{N}_{\gamma\mu} = \int\limits_K \phi_\gamma \frac{d\rho_0}{dz} \phi_\mu \, dK. \tag{35}$$

Substituting expansion (28) into the Hamiltonian (20) yields

$$H = \sum_K \frac{1}{2}\tilde{M}_{\alpha\beta}\left(\rho_0\underline{v}\right)_\alpha \cdot \left(\rho_0\underline{v}\right)_\beta + \frac{1}{2}\check{M}_{\alpha\beta}\rho_\alpha\rho_\beta - \mathrm{Ma}^2\,\check{M}_{\alpha\beta}\rho_\alpha p_\beta + \frac{1}{2}\,\mathrm{Ma}^4\,\check{M}_{\alpha\beta}p_\alpha p_\beta + \frac{1}{2}\,\mathrm{Ma}^2\,\tilde{M}_{\alpha\beta}p_\alpha p_\beta, \tag{36}$$

with

$$\tilde{M}_{\alpha\beta} = \int_K \frac{\phi_\alpha\phi_\beta}{\rho_0}\,\mathrm{d}K \qquad \text{and} \qquad \check{M}_{\alpha\beta} = \int_K \frac{\phi_\alpha\phi_\beta}{\rho_0 N^2}\,\mathrm{d}K. \tag{37}$$

The matrices (30), (34), (35) and (37) are calculated using Gaussian quadrature rules of the same order as the numerical solution.

A global formulation is introduced, using global coefficients $\underline{U}_i = (U, V, W)_i^T$, R_i and P_i. These represent the expansion coefficients from (28) and the index i runs over their global ranges. All elemental matrices extend to global matrices. The global formulation becomes

$$
\begin{aligned}
[F, G] = {} & \frac{\partial F}{\partial R_i}\left(\frac{\partial G}{\partial \underline{U}_j}\cdot\underline{DIV}_{kl}M_{ik}^{-1}M_{jl}^{-1} - \frac{\partial G}{\partial W_j}\check{N}_{kl}M_{ik}^{-1}M_{jl}^{-1}\right) \\
& - \frac{\partial G}{\partial R_i}\left(\frac{\partial F}{\partial \underline{U}_j}\cdot\underline{DIV}_{kl}M_{ik}^{-1}M_{jl}^{-1} - \frac{\partial F}{\partial W_j}\check{N}_{kl}M_{ik}^{-1}M_{jl}^{-1}\right) \\
& + \frac{\partial F}{\partial P_i}\left(\frac{\partial G}{\partial W_j}N_{kl}M_{ik}^{-1}M_{jl}^{-1} + \frac{1}{\mathrm{Ma}^2}\frac{\partial G}{\partial \underline{U}_j}\cdot\underline{DIV}_{kl}M_{ik}^{-1}M_{jl}^{-1}\right) \\
& - \frac{\partial G}{\partial P_i}\left(\frac{\partial F}{\partial W_j}N_{kl}M_{ik}^{-1}M_{jl}^{-1} + \frac{1}{\mathrm{Ma}^2}\frac{\partial F}{\partial \underline{U}_j}\cdot\underline{DIV}_{kl}M_{ik}^{-1}M_{jl}^{-1}\right)
\end{aligned}
\tag{38}
$$

with divergence operator

$$\underline{DIV}_{kl} = \underline{E}_{kl} - (1-\theta)\underline{G}_{kl}^{LL} - \theta\underline{G}_{kl}^{RL} + (1-\theta)\underline{G}_{kl}^{LR} + \theta\underline{G}_{kl}^{RR} \tag{39}$$

and global Hamiltonian

$$H = \frac{1}{2}\tilde{M}_{ij}\underline{U}_i\cdot\underline{U}_j + \frac{1}{2}\check{M}_{ij}R_iR_j - \mathrm{Ma}^2\,\check{M}_{ij}R_iP_j + \frac{1}{2}\,\mathrm{Ma}^4\,\check{M}_{ij}P_iP_j + \frac{1}{2}\,\mathrm{Ma}^2\,\tilde{M}_{ij}P_iP_j. \tag{40}$$

Note the correspondence of the formulation of the discrete bracket (38) with the continuum bracket (9). The discrete bracket (38) is a Poisson bracket: all four properties listed in Subsection 2.2 are satisfied. Skew-symmetry, linearity and the Leibniz rule follow directly from the bracket and the Jacobi identity follows after a straightforward but tedious calculation. The discretization method presented in this paper ensures more than anti-symmetry of the discrete bracket: it also ensures phase space conservation.

Substituting (40) into (38) yields the equations of motion

$$
\begin{aligned}
\dot{\underline{U}}_j = {} & \left(\tilde{M}_{il}\check{N}_{kl} + \mathrm{Ma}^2\,\check{M}_{il}N_{kl}\right)\hat{\underline{z}}R_lM_{ik}^{-1}M_{jl}^{-1} \\
& + \left(-\mathrm{Ma}^2\,\check{M}_{il}\check{N}_{kl}\hat{\underline{z}} - \mathrm{Ma}^4\,\check{M}_{il}N_{kl}\hat{\underline{z}} - \mathrm{Ma}^2\,\tilde{M}_{il}N_{kl}\hat{\underline{z}} - \tilde{M}_{il}\underline{DIV}_{kl}\right)P_lM_{ik}^{-1}M_{jl}^{-1} \\
\dot{R}_l = {} & \underline{U}_j\cdot\underline{DIV}_{jk}\tilde{M}_{ij}M_{lj}^{-1}M_{ik}^{-1} - W_j\check{N}_{jk}\tilde{M}_{ij}M_{lj}^{-1}M_{ik}^{-1} \\
\dot{P}_l = {} & W_j\tilde{M}_{ij}N_{jk}M_{lj}^{-1}M_{ik}^{-1} + \frac{1}{\mathrm{Ma}^2}\underline{U}_j\cdot\underline{DIV}_{jk}\tilde{M}_{ij}M_{lj}^{-1}M_{ik}^{-1},
\end{aligned}
\tag{41}
$$

where the dot denotes a time derivative.

3.3. Hamiltonian DGFEM discretization for linearized incompressible fluids

The discrete equations of motion for the incompressible case are obtained using Dirac's theory of constraints [29,30, 13]. Dirac's theory introduces Lagrange multipliers to enforce a constraint onto the Hamiltonian dynamics. In a consistent theory, the constraint must be preserved by the evolution of the system [13]. This leads to four possible outcomes: (i) the consistency requirement results in, module constraints, an equation of the form $1 = 0$. This implies an inconsistency, caused by enforcing a constraint that is inconsistent with the dynamics; (ii) it leads to an equation of the form $0 = 0$; this means the constraints and the dynamics are consistent and we are done; (iii) we obtain an expression for the unknown Lagrange

multiplier; (iv) we obtain a secondary constraint. This means the secondary constraint must also be preserved by the dynamics.

A Mach number analysis reveals that passing to the incompressible limit is equivalent to a zero perturbation pressure [32]. The zero pressure perturbation is enforced as primary constraint in every element:

$$D_k = M_{kl} P_l = 0. \tag{42}$$

A Lagrange multiplier λ_l is introduced to enforce the primary constraint. This constraint must be preserved in time. Hence, we require that

$$\dot{D}_k = [D_k, H] + \lambda_l [D_k, D_l] = 0. \tag{43}$$

From (38) it follows that $[D_k, D_l] = 0$ such that in (43) λ_l remains undetermined and a secondary constraint arises $[D_k, H] = 0$,

$$[D_k, H] = \tilde{M}_{jk} W_k M_{il} N_{kl} M_{ik}^{-1} M_{jl}^{-1} + \frac{1}{\text{Ma}^2} \tilde{M}_{jk} \underline{U}_k M_{il} \cdot \underline{DIV}_{kl} M_{ik}^{-1} M_{jl}^{-1} = 0. \tag{44}$$

The second term is a discrete version of the divergence of the velocity field. A difference in the order of the Mach number is present. Multiplying with Ma^2 and taking the limit of zero Mach number, $\text{Ma} \to 0$, the first term disappears. Therefore, we will use

$$L_k = \tilde{M}_{jk} \underline{U}_k \cdot \underline{DIV}_{kl} M_{jk}^{-1} = 0 \tag{45}$$

as second constraint, instead of (44).

Enforcing both constraints to be conserved in time simultaneously requires

$$
\begin{aligned}
0 &= \dot{D}_k = [D_k, H] + \mu_l [D_k, L_l], \\
0 &= \dot{L}_k = [L_k, H] + \lambda_l [L_k, D_l] + \mu_l [L_k, L_l].
\end{aligned}
\tag{46}
$$

From (38), $[L_k, L_l]$ is zero and $[D_k, H]$ is zero after using the constraints, again in the asymptotic limit $\text{Ma} = 0$. Equations (46) decouple and a solution to (46)-1 is $\mu_l = 0$. The other Lagrange multiplier is determined from (46)-2,

$$
\begin{aligned}
0 &= [L_k, H] + \lambda_l [L_k, D_l] \\
0 &= -\frac{\partial H}{\partial R_i} \left(\frac{\partial L_k}{\partial \underline{U}_j} \cdot \underline{DIV}_{kl} - \frac{\partial L_k}{\partial W_j} \check{N}_{kl} \right) M_{ik}^{-1} M_{jl}^{-1} - \frac{\partial H}{\partial P_i} \left(\frac{\partial L_k}{\partial W_j} N_{kl} + \frac{1}{\text{Ma}^2} \frac{\partial L_k}{\partial \underline{U}_j} \cdot \underline{DIV}_{kl} \right) M_{ik}^{-1} M_{jl}^{-1} \\
&\quad - \lambda_l \frac{\partial D_l}{\partial P_i} \left(\frac{\partial L_k}{\partial W_j} N_{kl} + \frac{1}{\text{Ma}^2} \frac{\partial L_k}{\partial \underline{U}_j} \cdot \underline{DIV}_{kl} \right) M_{ik}^{-1} M_{jl}^{-1} \\
&= \check{M}_{il} R_l \hat{\underline{z}} \cdot \tilde{M}_{ij} \underline{DIV}_{jk} M_{ij}^{-1} \left(\check{N}_{kl} + \text{Ma}^2 N_{kl} \right) \\
&\quad + \lambda_l \tilde{M}_{ij} \underline{DIV}_{jk} M_{ij}^{-1} \cdot \left(-\hat{\underline{z}} M_{il} N_{ml} - \frac{1}{\text{Ma}^2} M_{il} \underline{DIV}_{ml} \right) M_{ik}^{-1} M_{jl}^{-1},
\end{aligned}
\tag{47}
$$

where the constraint (42) was used. This equation determines the Lagrange multiplier λ_l. Again, a difference in the order of the Mach number is present. Scaling the Lagrange multiplier with the Mach number squared, such that $\tilde{\lambda}_l = \lambda_l / \text{Ma}^2$ and taking the limit of $\text{Ma} \to 0$ yields

$$0 = \check{M}_{il} R_l \hat{\underline{z}} \cdot \tilde{M}_{ij} \underline{DIV}_{jk} M_{ij}^{-1} \check{N}_{kl} - \tilde{\lambda}_l \tilde{M}_{ij} \underline{DIV}_{jk} M_{ij}^{-1} \cdot M_{il} \underline{DIV}_{ml} M_{ik}^{-1} M_{jl}^{-1}. \tag{48}$$

The Lagrange multiplier $\tilde{\lambda}_l$ plays the role of pressure. If we define Θ_l as $\tilde{M}_{il} \Theta_l M_{il} = \tilde{\lambda}_l = \lambda_l / \text{Ma}^2$, Θ_l is the discrete pressure.

The resulting discrete, linear, incompressible Hamiltonian dynamics are given by

$$
\begin{aligned}
\frac{dF}{dt} &= -\left(\frac{\partial H}{\partial W_j} \frac{\partial F}{\partial R_i} - \frac{\partial F}{\partial W_j} \frac{\partial H}{\partial R_i} \right) \check{N}_{kl} M_{ik}^{-1} M_{jl}^{-1} - \tilde{M}_{il} \Theta_l M_{il}^{-1} \frac{\partial F}{\partial \underline{U}_j} \cdot \underline{DIV}_{ml} M_{jm}^{-1} \\
0 &= \check{M}_{il} R_l \hat{\underline{z}} \cdot \tilde{M}_{ij} \underline{DIV}_{jk} M_{ij}^{-1} \check{N}_{kl} - \tilde{M}_{ij} \underline{DIV}_{jk} M_{ij}^{-1} \tilde{M}_{il} \Theta_l M_{il} \cdot M_{il} \underline{DIV}_{ml} M_{ik}^{-1} M_{jl}^{-1}
\end{aligned}
\tag{49}
$$

with constrained Hamiltonian

$$H = \frac{1}{2} \tilde{M}_{ij} \underline{U}_i \cdot \underline{U}_j + \frac{1}{2} \check{M}_{ij} R_i R_j. \tag{50}$$

The equations of motion arising from the dynamics (49) are

$$\dot{\underline{U}}_j = \hat{\underline{z}} \check{M}_{il} \check{N}_{kl} R_l M_{ik}^{-1} M_{jl}^{-1} - \tilde{M}_{il} \Theta_l M_{il}^{-1} \underline{DIV}_{ml} M_{jm}^{-1}$$
$$\dot{R}_l = -\tilde{M}_{ij} \check{N}_{jk} W_j M_{jl}^{-1} M_{ik}^{-1}, \tag{51}$$

combined with (49)-2.

3.4. Hamiltonian DGFEM discretization for Euler–Boussinesq fluids

The Boussinesq approximation consists of replacing the background density by a constant background reference density, ρ^*, in the inertia terms and the definition of the buoyancy frequency. We nondimensionalize such that $\rho^* = 1$. The discrete momenta, $\underline{U}$, are redefined to

$$\underline{U} = (\underline{v})_h. \tag{52}$$

The Hamiltonian structure is slightly modified. From (10) it follows that the first term, the kinetic energy term, of the Hamiltonian no longer is a function of the background density. Since the definition of the buoyancy frequency changed, see (6), the potential energy term, (37), is also changed. The varying background density is replaced by a constant reference density:

$$\check{M}_{\alpha\beta} = \int\limits_K \frac{\phi_\alpha \phi_\beta}{N^2} \, dK. \tag{53}$$

The discrete Hamiltonian (50) is changed to

$$H = \frac{1}{2} M_{ij} \underline{U}_i \cdot \underline{U}_j + \frac{1}{2} \check{M}_{ij} R_i R_j. \tag{54}$$

In the Poisson bracket (49) the $\underline{U}_j$ are replaced by their new definition. Since the first term in the Hamiltonian no longer depends on the background density, the numerical fluxes (24) show that the discrete divergence operators $\underline{DIV}_{ml}$ no longer depend on ρ_0. The equations of motion obtained from the bracket are

$$\dot{\underline{U}}_j = \hat{\underline{z}} \check{M}_{il} \check{N}_{kl} R_l M_{ik}^{-1} M_{jl}^{-1} - \Theta_l \underline{DIV}_{ml} M_{jm}^{-1},$$
$$\dot{R}_l = -\check{N}_{jk} W_j M_{lk}^{-1}. \tag{55}$$

4. Time integrator

The derivation of the discrete equations of motion ensured that the Hamiltonian structure is preserved by the spatial discretization. We used a symplectic time integrator to ensure the Hamiltonian structure is preserved in time [31]. As symplectic time integrator the implicit midpoint scheme was chosen, as this is the most simple time integrator that conserves quadratic invariants.

4.1. Linearized compressible stratified fluids

Applying the modified midpoint scheme to (41) yields, after scaling such that $\text{Ma} = 1$,

$$\frac{\underline{U}_j^{n+1} - \underline{U}_j^n}{\Delta t} = \left(\check{M}_{il} \check{N}_{kl} + \check{M}_{il} N_{kl} \right) \hat{\underline{z}} \frac{R_l^{n+1} + R_l^n}{2} M_{ik}^{-1} M_{jl}^{-1}$$
$$+ \left(-\check{M}_{il} \check{N}_{kl} \hat{\underline{z}} - \check{M}_{il} N_{kl} \hat{\underline{z}} - \tilde{M}_{il} N_{kl} \hat{\underline{z}} - \tilde{M}_{il} \underline{DIV}_{kl} \right) \frac{P_l^{n+1} + P_l^n}{2} M_{ik}^{-1} M_{jl}^{-1},$$
$$\frac{R_l^{n+1} - R_l^n}{\Delta t} = \frac{\underline{U}_j^{n+1} + \underline{U}_j^n}{2} \cdot \underline{DIV}_{jk} \tilde{M}_{ij} M_{lj}^{-1} M_{ik}^{-1} - \frac{W_j^{n+1} + W_j^n}{2} \check{N}_{jk} \tilde{M}_{ij} M_{lj}^{-1} M_{ik}^{-1}, \tag{56}$$
$$\frac{P_l^{n+1} - P_l^n}{\Delta t} = \frac{W_j^{n+1} + W_j^n}{2} \tilde{M}_{ij} N_{jk} M_{lj}^{-1} M_{ik}^{-1} + \frac{\underline{U}_j^{n+1} + \underline{U}_j^n}{2} \cdot \underline{DIV}_{jk} \tilde{M}_{ij} M_{lj}^{-1} M_{ik}^{-1}.$$

Multiplying (56)-1 with $\frac{1}{2} \tilde{M}_{ij} \left(\underline{U}_i^{n+1} + \underline{U}_i^n \right)$, (56)-2 with $\left[\frac{1}{2} \check{M}_{kl} \left(R_k^{n+1} + R_k^n \right) - \frac{1}{2} \check{M}_{kl} \left(P_k^{n+1} + P_k^n \right) \right]$ and (56)-3 with $\left[-\frac{1}{2} \check{M}_{kl} \left(R_k^{n+1} + R_k^n \right) + \frac{1}{2} \check{M}_{kl} \left(P_k^{n+1} + P_k^n \right) + \frac{1}{2} \tilde{M}_{kl} \left(P_k^{n+1} + P_k^n \right) \right]$, and adding over all elements yields $(H^{n+1} - H^n)/\Delta t = 0$. So the numerical scheme (56) is exactly energy conserving.

4.2. Linearized incompressible stratified fluids

Applying the modified midpoint scheme to (51) yields

$$
\begin{aligned}
\frac{\underline{U}_j^{n+1} - \underline{U}_j^n}{\Delta t} &= \hat{\underline{z}} \tilde{M}_{il} \check{N}_{kl} \frac{R_l^{n+1} + R_l^n}{2} M_{ik}^{-1} M_{jl}^{-1} - \tilde{M}_{il} \Theta_l^{n+1} M_{il}^{-1} \underline{DIV}_{ml} M_{jm}^{-1}, \\
\frac{R_l^{n+1} - R_l^n}{\Delta t} &= -\tilde{M}_{ij} \check{N}_{jk} \frac{W_j^{n+1} + W_j^n}{2} M_{lj}^{-1} M_{ik}^{-1}, \\
\tilde{M}_{ij} \underline{DIV}_{jk} M_{ij}^{-1} \cdot \hat{\underline{z}} \tilde{M}_{il} \check{N}_{kl} \frac{R_l^{n+1} + R_l^n}{2} M_{ik}^{-1} M_{jl}^{-1} &= \tilde{M}_{ij} \underline{DIV}_{jk} M_{ij}^{-1} \tilde{M}_{il} \Theta_l^{n+1} M_{il}^{-1} M_{jm}^{-1} \cdot \underline{DIV}_{ml}.
\end{aligned}
\tag{57}
$$

Assume that the velocity at time level n is divergence-free, so $\tilde{M}_{ij} \underline{DIV}_{jk} M_{ij}^{-1} \cdot \underline{U}_j^n = 0$. To show that the velocity stays divergence-free, multiply (57)-1 by $\tilde{M}_{ij} \underline{DIV}_{jk} M_{ij}^{-1}$ to obtain

$$
\begin{aligned}
\tilde{M}_{ij} \underline{DIV}_{jk} M_{ij}^{-1} \cdot \frac{\underline{U}_j^{n+1} - \underline{U}_j^n}{\Delta t} &= \frac{1}{\Delta t} \tilde{M}_{ij} \underline{DIV}_{jk} M_{ij}^{-1} \cdot \underline{U}_j^{n+1} = \\
\tilde{M}_{ij} \underline{DIV}_{jk} M_{ij}^{-1} \cdot \left(\hat{\underline{z}} \tilde{M}_{il} \check{N}_{kl} \frac{R_l^{n+1} + R_l^n}{2} M_{ik}^{-1} M_{jl}^{-1} - \tilde{M}_{il} \Theta_l^{n+1} M_{il}^{-1} \underline{DIV}_{ml} M_{jm}^{-1} \right) &= 0,
\end{aligned}
\tag{58}
$$

by (57)-3. To show that the Hamiltonian is preserved, multiply (57)-1 with $\frac{1}{2} \tilde{M}_{ij} \left(\underline{U}_i^{n+1} + \underline{U}_i^n \right)$ and (57)-2 with $\frac{1}{2} \check{M}_{kl} \left(R_k^{n+1} + R_k^n \right)$ and add over all elements to obtain

$$
\frac{H^{n+1} - H^n}{\Delta t} = -\frac{1}{2} \tilde{M}_{ij} \left(\underline{U}_i^{n+1} + \underline{U}_i^n \right) \cdot \underline{DIV}_{ml} \tilde{M}_{il} \Theta_l^{n+1} M_{il}^{-1} M_{jm}^{-1} = 0,
\tag{59}
$$

by the zero divergence of the velocity field. So the numerical scheme (57) conserves the divergence of the velocity field and, if the divergence is zero, the energy.

4.3. Euler–Boussinesq fluids

Applying the modified midpoint scheme to (55) yields

$$
\begin{aligned}
\frac{\underline{U}_j^{n+1} - \underline{U}_j^n}{\Delta t} &= \hat{\underline{z}} \tilde{M}_{il} \check{N}_{kl} \frac{R_l^{n+1} + R_l^n}{2} M_{ik}^{-1} M_{jl}^{-1} - \Theta_l^{n+1} \underline{DIV}_{ml} M_{jm}^{-1}, \\
\frac{R_l^{n+1} - R_l^n}{\Delta t} &= -\check{N}_{jk} \frac{W_j^{n+1} + W_j^n}{2} M_{lk}^{-1}, \\
\underline{DIV}_{jk} \cdot \hat{\underline{z}} \tilde{M}_{il} \check{N}_{kl} \frac{R_l^{n+1} + R_l^n}{2} M_{ik}^{-1} M_{jl}^{-1} &= \underline{DIV}_{jk} \Theta_l^{n+1} M_{jm}^{-1} \cdot \underline{DIV}_{ml}.
\end{aligned}
\tag{60}
$$

The scheme is again exactly energy conserving and exactly velocity-divergence conserving.

4.4. Initial conditions

The last two discretizations, (57) and (60), conserve the discrete divergence of the velocity exactly. Even though the continuous initial condition is divergence-free, the discrete initial condition is not: the projection of the initial, divergence-free velocity field on the chosen discontinuous Galerkin finite element space only satisfies discrete zero-divergence up to the order of accuracy. A new initial velocity, $\left(\underline{U}_k^0\right)_0$, is sought such that the discrete divergence of the velocity, (45), is zero, $\tilde{M}_{jk} \left(\underline{U}_k^0\right)_0 \cdot \underline{DIV}_{kl} M_{jk}^{-1} = 0$, and the distance between the old initial velocity, $\left(\underline{U}_k^0\right)_*$, and the new initial velocity, $\left\| \left(\underline{U}_k^0\right)_0 - \left(\underline{U}_k^0\right)_* \right\|$, is minimal. A projection of the vector $\left(\underline{U}_k^0\right)_*$ on the space kernel of the discrete divergence matrix operator is sought. Denote this projection with $\pi(\cdot)$. Then

$$
\left(\underline{U}_k^0\right)_0 = \pi \left(\left(\underline{U}_k^0\right)_* \right) = \left(\underline{U}_k^0\right)_* + \left(\underline{U}_k^0\right)_\perp,
\tag{61}
$$

where $\left(\underline{U}_k^0\right)_\perp$ is perpendicular to the kernel. Applying the discrete divergence operator to (61) yields (cf. [13])

$$
0 = \tilde{M}_{jk} \left(\underline{U}_k^0\right)_* \cdot \underline{DIV}_{kl} M_{jk}^{-1} + \tilde{M}_{jk} \left(\underline{U}_k^0\right)_\perp \cdot \underline{DIV}_{kl} M_{jk}^{-1},
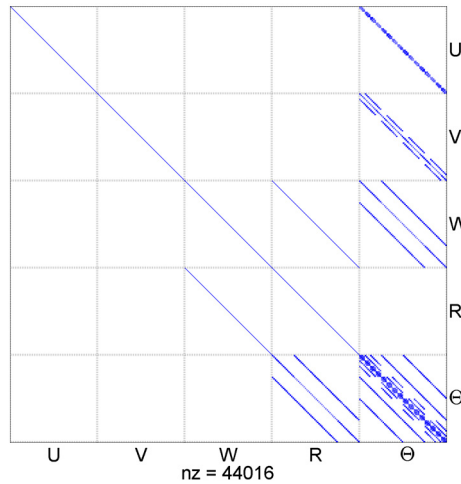\tag{62}
$$

Fig. 1. The P-matrix for a three-dimensional (incompressible) Euler–Boussinesq fluid. All nonzero elements are shown. The letters indicate the discrete variables. nz denotes the number of nonzero entries. The number of elements in each direction was four and the polynomial order was two.
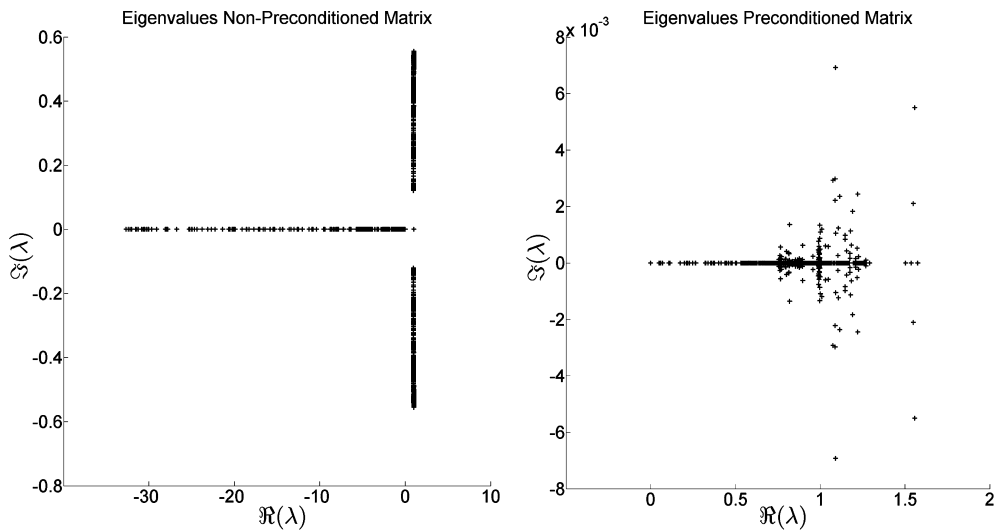

Fig. 2. The eigenvalues λ of the matrix P, with (right picture) and without (left picture) preconditioning. The ILU preconditioner moves the eigenvalues closer together and makes the real part of the eigenvalues positive. The matrix P was obtained from the test problem discussed in Subsection 5.4 with 128 elements and a polynomial order of two.

where the discrete divergence of the new initial velocity, $\left(\underline{U}_k^0\right)_0$, being zero, was used. (62) is solved for $\left(\underline{U}_k^0\right)_\perp$ via a least-square approximation. Then the new, divergence-free, initial velocity, $\left(\underline{U}_k^0\right)_0$, is computed with (61). Now that the initial velocity is divergence-free, the solution stays divergence-free due to the conservation of divergence of the velocity as a result of the Hamiltonian dynamics and the time integration.

4.5. Properties of the discrete system

From (56), (57) or (60) global matrices are assembled. All terms multiplying the coefficients at the next time step are collected in a matrix P and all terms multiplying the coefficients at the current time step are collected in a matrix Q. The matrices P and Q are time independent. Denoting the vector of coefficients with X the constructed system is

$$PX^{n+1} = QX^n. \tag{63}$$

Fig. 1 shows the P-matrix for a three-dimensional (incompressible) Euler–Boussinesq fluid. The symbols on the right and the bottom correspond to the discrete variables. The exact preservation of the Hamiltonian dynamics as well as the constraints make the system unconditionally stable.

The discretizations were implemented in the hpGEM C++ software framework [20]. The computational linear algebra demands were handled by using PETSc [19]. This tool kit PETSc, a "Portable, Extensible Toolkit for Scientific Computation",

Table 1

Extreme eigenvalues of the non-preconditioned and preconditioned matrix.

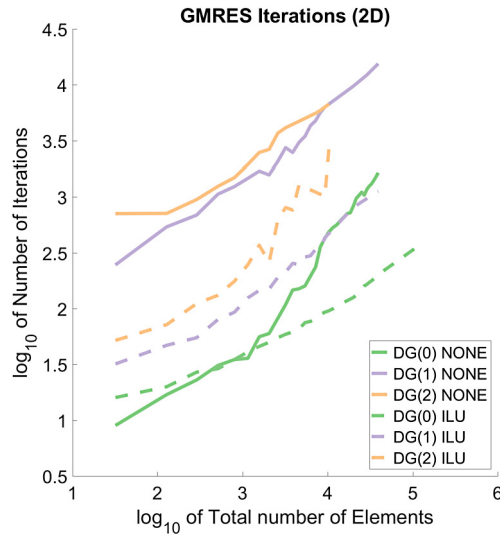| Matrix	$\max \Re(\lambda)$	$\min \Re(\lambda)$	$\max \Im(\lambda)$	$\max |\lambda|$	$\min |\lambda|$
Non-preconditioned	1.0000	-32.6746	0.5554	32.6746	~ 0
Preconditioned	1.5753	~ 0	0.0069	1.5753	~ 0

Fig. 3. The number of iterations per time step using GMRES with (dashed lines) and without (solid lines) preconditioning as a function of the total number of elements for a two-dimensional problem. DG(N_p) means using polynomials up to and including order N_p. For DG(1) and DG(2) the ILU preconditioner reduces the number of iterations by a factor of ten. For small problem sizes, preconditioning for DG(0) does not decrease the number of iterations. For larger problem sizes, preconditioning for DG(0) does decrease the number of iterations. The time step Δt was equal to the spatial step Δx.

consists of a number of sparse matrix storage routines and both iterative and direct sparse linear solvers. A GMRES iterative solver was used to reach the desired tolerance of 10^{-14}. To speed up the computations an ILU preconditioner was added.

The performance of the GMRES iterative solver depends on the spectrum of the matrix P. The eigenvalues λ obtained from the matrix P, for the test problem discussed in Subsection 5.4, are shown in Fig. 2. In Table 1 the extreme eigenvalues are presented. In this case, there are two eigenvalues near $(0, 0)$, originating from the elliptic equations (60)-3, corresponding to the bottom right block matrix in Fig. 1. To improve the spectrum of the matrices and to decrease the number of iterations in the iterative solver, we applied an ILU preconditioner. Preconditioning the matrix moved the eigenvalues closer together and made the real part of the eigenvalues positive. The left image of Fig. 2 shows the eigenvalues before preconditioning and the right image of Fig. 2 shows the eigenvalues after preconditioning.

The number of iterations of the GMRES iterative solver per time step is shown in Fig. 3. The number of iterations required by the GMRES iterative solver to reach the desired tolerance of 10^{-14} is shown as a function of the total number of elements for the two-dimensional problem discussed in Subsection 5.4. In general, the use of a preconditioner decreases the number of required iterations to reach convergence by a factor 10. The improvement of the spectrum, shown in Fig. 2, makes the discrete system better suited to be solved using the GMRES iterative solver.

5. Tests of the numerical scheme

In this section we perform several tests of the numerical scheme. Although our main goal is to simulate internal gravity waves in an incompressible fluid, including the Boussinesq approximation, we have also performed tests for compressible fluids and incompressible fluids, excluding the Boussinesq approximation. These extra test cases verified the approaches and techniques used and provided intermediate check-points during the development. Each test consisted of two parts: a convergence analysis of the error, found by comparing our numerical solution to available exact solutions, and a check on the energy conservation law. The first two tests, in Subsections 5.1 and 5.2, handle compressible fluids in cuboids. The first test concerns a modal solution for internal gravity waves and the second test concerns Lamb waves. These tests provide a proof of concept and show that our numerical model can handle three-dimensional geometries. The third test, found in Subsection 5.3, concerns a modal solution for internal gravity waves in an incompressible fluid in a square. Here, the velocity field must remain divergence-free. The remaining tests all concern the discretization of the Euler–Boussinesq equations (5). In Subsection 5.4 a beam of internal gravity waves is simulated. This beam is a superposition of modes; each of these modes travels at its own phase speed, while the beam stays in place. In Subsection 5.5 non-uniform stratification is considered. The stratification is chosen such that in the upper part of the water column internal gravity waves can propagate while in
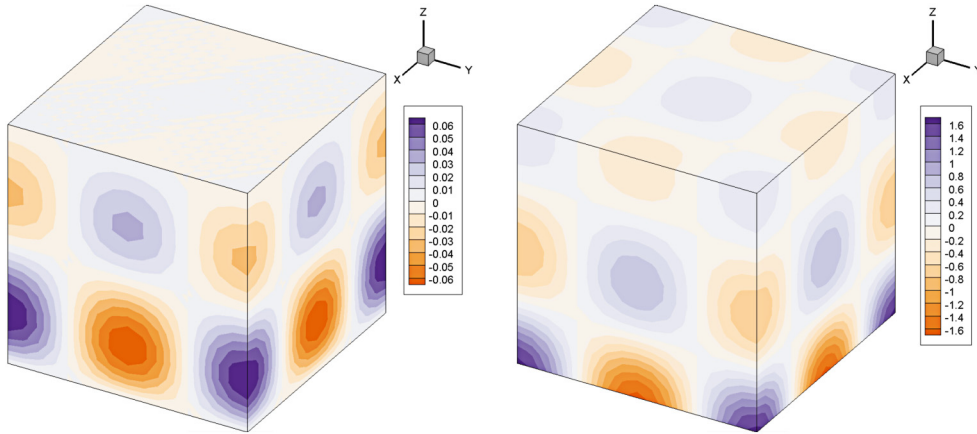
Fig. 4. The numerical solution for three-dimensional waves in a stratified compressible fluid. The left image shows the vertical velocity and the right image the pressure. The number of elements in each direction was 16 and the polynomial order was three.

the lower part of the water column they cannot. In Subsection 5.6 we demonstrate the ability of the code to simulate wave attractors, the limit cycles of internal gravity waves. For all reported test cases, $\theta = 1/2$ was used in the numerical flux. For other constant values of $0 \le \theta \le 1$ the results are similar [32].

5.1. Compressible stratified waves with solid wall boundary conditions

Consider a linear compressible stratified fluid with a background density field of $\rho_0 = \exp(-3z)$ in a rectangular domain $\Omega = [0, 1]^3$ with solid walls. A solution to (2), after scaling such that $g = c_0^2 = 1$ is

$$\rho_0 u = \exp\left(-\frac{3}{2}z\right) \frac{2\pi}{\sigma^2 - 8\pi^2} \left[2\pi \cos(2\pi z) + \sin(2\pi z)\right] \sin(2\pi x) \cos(2\pi y) \sin(\sigma t + 0.1),$$

$$\rho_0 v = \exp\left(-\frac{3}{2}z\right) \frac{2\pi}{\sigma^2 - 8\pi^2} \left[2\pi \cos(2\pi z) + \sin(2\pi z)\right] \cos(2\pi x) \sin(2\pi y) \sin(\sigma t + 0.1),$$

$$\rho_0 w = \exp\left(-\frac{3}{2}z\right) \sin(2\pi z) \cos(2\pi x) \cos(2\pi y) \sin(\sigma t + 0.1), \tag{64}$$

$$\rho = \exp\left(-\frac{3}{2}z\right) \frac{\sigma}{\sigma^2 - 8\pi^2} \cos(2\pi x) \cos(2\pi y) \left[2\pi \cos(2\pi z) - \left(\frac{3}{2} - \frac{16\pi^2}{\sigma^2}\right) \sin(2\pi z)\right] \cos(\sigma t + 0.1),$$

$$p = \exp\left(-\frac{3}{2}z\right) \frac{\sigma}{\sigma^2 - 8\pi^2} \left[\sin(2\pi z) + 2\pi \cos(2\pi z)\right] \cos(2\pi x) \cos(2\pi y) \cos(\sigma t + 0.1)$$

with frequency σ, obtained from

$$2\sigma^2 = 12\pi^2 + \frac{9}{4} + \sqrt{\left(12\pi^2 + \frac{9}{4}\right)^2 - 64\pi^2}. \tag{65}$$

This solution describes a standing pattern of internal gravity waves.

The numerical discretization is initialized at time $t = 0$. Fig. 4 shows the numerical solution after three periods. By comparing the numerical solution with the exact solution (64) we determined the L^2-error and order of convergence of the numerical solution after three periods. To ensure the solution is nonzero, we added a phase shift in (64). Table 2 presents the L^2-error and order of convergence for the different variables as a function of the number of elements in a direction, K, and the polynomial order of the approximation, N_p. With decreasing element size, we decrease the time step such that it has the same order of convergence as the spatial discretization. For an increasing number of elements and an increasing polynomial order, the error in the numerical solution decreases. The results for the different variables are similar. The total energy is conserved up to machine precision. Fig. 5 shows the error in the total energy for 100 periods for a polynomial order one, $N_p = 1$. The discretization ensures conservation of energy. The total mass (the summation of all density perturbations) and momentum in three directions are also conserved up to machine precision.

Table 2

L^2-error and order of convergence of the numerical solution after three periods for three-dimensional waves in a solid wall domain for a stratified compressible fluid. The number of elements in each direction, K, is varied from four to 64. The polynomial order, N_p, is varied from zero to three. Due to symmetry the error in the horizontal velocities is equal.

| $N_p = 0$	$\rho_0 u, \rho_0 v$		$\rho_0 w$		ρ		p	
K	L^2-error	Order	L^2-error	Order	L^2-error	Order	L^2-error	Order
4	2.63E−1	–	1.93E−1	–	1.13E+0	–	1.21E+0	–
8	5.70E−1	−1.11	5.49E−1	−1.11	1.07E+0	0.07	1.08E+0	0.16
16	2.60E−1	1.13	2.50E−1	1.13	3.47E−1	1.63	3.49E−1	1.63
32	6.88E−2	1.92	6.75E−2	1.92	1.74E−1	0.99	1.76E−1	0.99
64	1.81E−2	1.93	1.82E−2	1.93	8.74E−2	1.00	8.79E−2	1.00
$N_p = 1$	$\rho_0 u, \rho_0 v$		$\rho_0 w$		ρ		p	
K	L^2-error	Order	L^2-error	Order	L^2-error	Order	L^2-error	Order
4	2.67E−1	–	4.21E−1	–	8.74E−1	–	8.77E−1	–
8	9.49E−2	1.49	1.03E−1	1.49	4.60E−1	0.93	4.69E−1	0.90
16	5.08E−2	0.90	5.72E−2	0.90	1.96E−1	1.23	2.01E−1	1.22
32	2.55E−2	0.99	3.38E−2	0.99	8.62E−2	1.19	8.85E−2	1.18
$N_p = 2$	$\rho_0 u, \rho_0 v$		$\rho_0 w$		ρ		p	
K	L^2-error	Order	L^2-error	Order	L^2-error	Order	L^2-error	Order
4	1.94E−1	–	2.20E−1	–	5.01E−1	–	4.87E−1	–
8	2.35E−2	3.05	2.35E−2	3.05	7.20E−2	2.80	7.30E−2	2.74
16	7.30E−3	1.68	5.42E−3	1.68	2.90E−2	1.31	2.61E−2	1.49
32	5.78E−4	3.66	3.78E−4	3.66	7.97E−3	1.86	7.29E−3	1.84
$N_p = 3$	$\rho_0 u, \rho_0 v$		$\rho_0 w$		ρ		p	
K	L^2-error	Order	L^2-error	Order	L^2-error	Order	L^2-error	Order
4	4.54E−2	–	5.86E−2	–	2.78E−1	–	2.87E−1	–
8	7.73E−3	2.56	7.71E−3	2.56	3.08E−2	3.17	2.68E−2	3.42
16	9.68E−4	3.00	1.17E−3	3.00	2.55E−3	3.59	1.86E−3	3.85
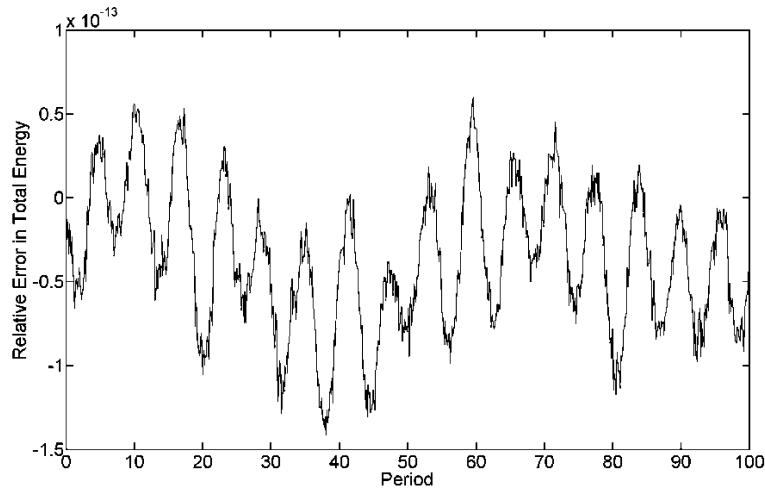
Fig. 5. The relative error in total energy for the numerical solution for three-dimensional waves in a solid wall domain for a stratified compressible fluid during 100 periods. The total energy was 0.1805. Also the mass and momenta in three directions were conserved up to machine precision. The number of elements in each direction and the number of time steps in a period was 8 and the polynomial order was one.

5.2. Lamb waves with mixed boundary conditions

Consider a linear compressible stratified fluid with a background density field of $\rho_0 = \exp(-3z)$ in a rectangular domain $\Omega = [0, 1]^3$ which is periodic in the horizontal directions and has solid walls in the vertical direction. A solution to (2), with $g = c_0^2 = 1$, is

Table 3

L^2-error and order of convergence of the numerical solution after three periods for three-dimensional Lamb waves for a stratified compressible fluid. Due to symmetry the error in the horizontal velocities is equal.

| $N_p = 0$	u, v		w		ρ		p	
K	L^2-error	Order	L^2-error	Order	L^2-error	Order	L^2-error	Order
4	9.68E−1	–	1.72E−1	–	1.35E+0	–	1.37E+0	–
8	1.46E+0	−0.59	1.26E−1	−0.59	2.04E+0	−0.60	2.06E+0	−0.59
16	5.03E−1	1.53	6.34E−2	1.53	7.01E−1	1.54	7.11E−1	1.53
32	1.74E−1	1.53	2.61E−2	1.53	2.43E−1	1.53	2.45E−1	1.53
64	7.28E−2	1.26	1.28E−2	1.26	1.03E−1	1.24	1.03E−1	1.25
$N_p = 1$	u, v		w		ρ		p	
K	L^2-error	Order	L^2-error	Order	L^2-error	Order	L^2-error	Order
4	7.29E−1	–	6.87E−1	–	1.12E+0	–	1.12E+0	–
8	2.74E−1	1.41	1.18E−1	1.41	4.38E−1	1.35	4.35E−1	1.37
16	9.82E−2	1.48	4.90E−2	1.48	1.80E−1	1.28	1.78E−1	1.29
32	4.02E−2	1.29	2.15E−2	1.29	7.02E−2	1.36	6.96E−2	1.35
$N_p = 2$	u, v		w		ρ		p	
K	L^2-error	Order	L^2-error	Order	L^2-error	Order	L^2-error	Order
4	3.27E−1	–	1.64E−1	–	4.82E−1	–	4.76E−1	–
8	6.71E−2	2.28	4.11E−2	2.28	9.40E−2	2.36	8.94E−2	2.41
16	1.22E−2	2.46	9.55E−3	2.46	1.80E−2	2.39	1.52E−2	2.55
32	2.04E−3	2.58	2.26E−3	2.58	3.20E−3	2.49	2.14E−3	2.83
$N_p = 3$	u, v		w		ρ		p	
K	L^2-error	Order	L^2-error	Order	L^2-error	Order	L^2-error	Order
4	8.52E−2	–	1.25E−1	–	1.23E−1	–	1.16E−1	–
8	8.60E−3	3.31	1.63E−2	3.31	1.23E−2	3.33	6.81E−3	4.10
16	1.58E−3	2.44	1.77E−3	2.44	2.06E−3	2.57	1.28E−3	2.41
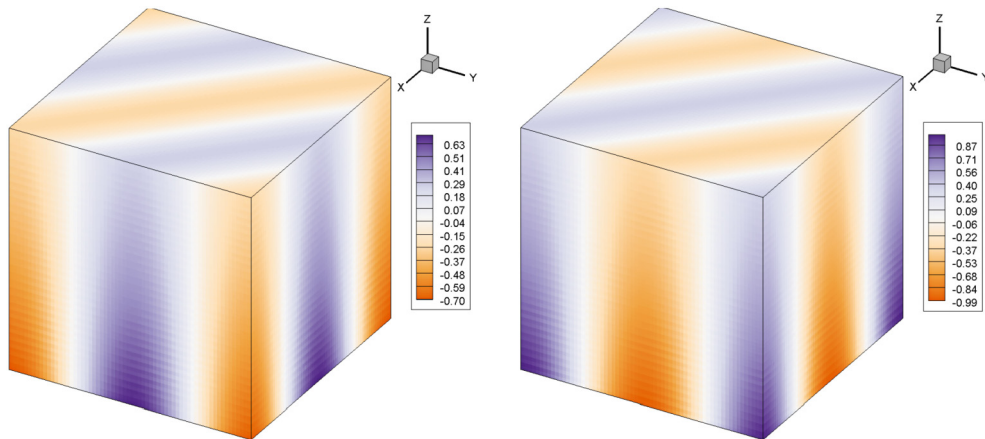
Fig. 6. The numerical solution for the three-dimensional Lamb waves in a stratified compressible fluid after three periods. The left image shows the horizontal velocity in the x-direction and the right image the density. The number of elements in each direction was 64 and the polynomial order was zero.

$$u = v = -\frac{1}{\sqrt{2}} \exp(-z) \cos\left(2\pi x + 2\pi y + 2\sqrt{2}\pi t\right),$$
$$w = 0, \tag{66}$$
$$\rho = p = \exp(-z) \cos\left(2\pi x + 2\pi y + 2\sqrt{2}\pi t\right).$$

Table 3 presents the L^2-error and order of convergence of the numerical solution after three periods. The total energy is conserved up to machine precision. The mass and momentum in three directions are also conserved up to machine precision. Fig. 6 shows the numerical solution after three periods.

Table 4
L^2-error and order of convergence of the numerical solution after three periods for two-dimensional waves in a solid wall domain for a stratified incompressible fluid.

$N_p = 0$ K	$\rho_0 u$		$\rho_0 w$		ρ		P	
	L^2-error	Order	L^2-error	Order	L^2-error	Order	L^2-error	Order
4	7.34E−1	–	6.64E−1	–	1.43E+0	–	1.29E−1	–
8	8.31E−2	3.14	1.30E−1	2.36	7.76E−1	0.88	6.72E−2	0.95
16	3.39E−2	1.29	5.98E−2	1.12	3.76E−1	1.05	3.13E−2	1.10
32	1.67E−2	1.02	2.94E−2	1.03	1.87E−1	1.01	1.54E−2	1.02
64	8.28E−3	1.01	1.46E−2	1.01	9.35E−2	1.00	7.70E−3	1.00
128	4.13E−3	1.00	7.29E−3	1.00	4.67E−2	1.00	3.84E−3	1.00
$N_p = 1$ K	$\rho_0 u$		$\rho_0 w$		ρ		P	
	L^2-error	Order	L^2-error	Order	L^2-error	Order	L^2-error	Order
4	7.40E−2	–	1.90E−1	–	8.67E−1	–	6.74E−2	–
8	6.48E−2	0.19	5.60E−2	1.76	2.52E−1	1.78	2.42E−2	1.48
16	4.02E−2	0.69	2.60E−2	1.11	1.12E−1	1.17	1.07E−2	1.17
32	1.99E−2	1.01	9.76E−3	1.41	4.95E−2	1.18	5.18E−3	1.05
$N_p = 2$ K	$\rho_0 u$		$\rho_0 w$		ρ		P	
	L^2-error	Order	L^2-error	Order	L^2-error	Order	L^2-error	Order
4	1.55E−1	–	1.74E−1	–	6.23E−1	–	2.92E−2	–
8	3.11E−2	2.32	6.12E−2	1.51	8.88E−2	2.81	6.09E−3	2.26
16	7.89E−3	1.98	1.51E−2	2.02	1.72E−2	2.37	1.40E−3	2.12
$N_p = 3$ K	$\rho_0 u$		$\rho_0 w$		ρ		P	
	L^2-error	Order	L^2-error	Order	L^2-error	Order	L^2-error	Order
4	2.35E−1	–	2.63E−1	–	3.54E−1	–	1.34E−2	–
8	1.19E−2	4.31	1.95E−2	3.75	1.68E−2	4.40	5.89E−4	4.50
16	8.22E−4	3.85	2.46E−3	2.98	3.64E−3	2.21	2.84E−5	4.37

5.3. Waves in an incompressible stratified fluid with solid wall boundary conditions

Consider a linear incompressible stratified fluid with a background density field of $\rho_0 = \exp(-2z)$ in a rectangular domain $\Omega = [0, 1]^2$ with solid walls. A solution to (4), after scaling such that $g = 1$, is

$$\rho_0 u = -\exp(-z)\left[\frac{1}{2\pi}\sin(2\pi z) + \cos(2\pi z)\right]\sin(2\pi x)\sin(\sigma t + 0.1),$$

$$\rho_0 w = \exp(-z)\sin(2\pi z)\cos(2\pi x)\sin(\sigma t + 0.1),$$

$$\rho = -\exp(-z)\frac{2}{\sigma}\sin(2\pi z)\cos(2\pi x)\cos(\sigma t + 0.1),$$

$$P = -\exp(-z)\left[\frac{\sigma}{4\pi^2}\sin(2\pi z) + \frac{\sigma}{2\pi}\cos(2\pi z)\right]\cos(2\pi x)\cos(\sigma t + 0.1)$$

(67)

with frequency σ, obtained from

$$\sigma^2 = \frac{8\pi^2}{1 + 8\pi^2}.$$

(68)

Table 4 presents the L^2-error and order of convergence of the numerical solution after three periods. The total energy is conserved up to machine precision. Fig. 7 shows the maximum error (L_∞-error) in the divergence of the velocity for 100 periods for a polynomial order zero. Fig. 8 shows the numerical solution after three periods.

5.4. Beam of internal gravity waves

Consider a linear incompressible Euler–Boussinesq fluid with a background density field of $\rho_0 = \exp(-2z)$ in a rectangular domain $\Omega = [0, 2] \times [0, 1]$, which is periodic in the horizontal direction and has solid walls in the vertical direction. A solution to (5), after scaling such that $g = 1$, is

$$u = \sum_{n=1}^{10}\cos(n\pi z)\cos(n\pi x - t), \qquad \rho = \sum_{n=1}^{10}2\sin(n\pi z)\cos(n\pi x - t),$$

$$w = \sum_{n=1}^{10}\sin(n\pi z)\sin(n\pi x - t), \qquad P = \sum_{n=1}^{10}\frac{1}{n\pi}\cos(n\pi z)\cos(n\pi x - t).$$
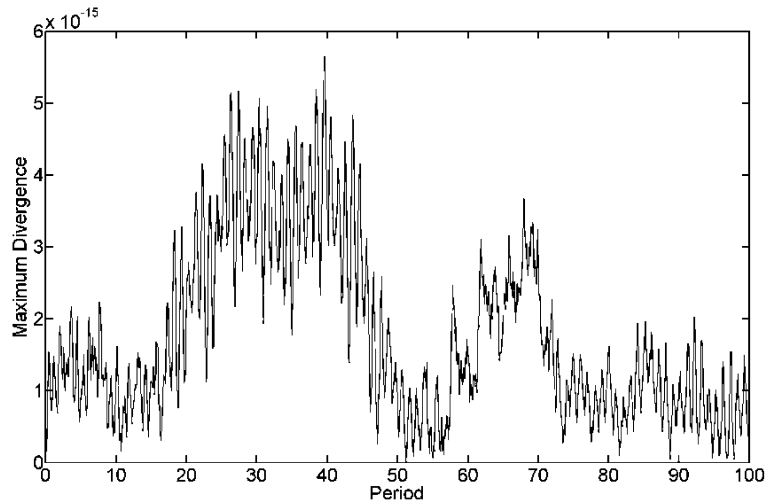
(69)

Fig. 7. The maximum divergence of the velocity field of the numerical solution for two-dimensional waves in a solid wall domain for a stratified incompressible fluid during 100 periods. Energy is also preserved up to machine precision. The number of elements in each direction and the number of time steps in a period was 16 and the polynomial order was zero.
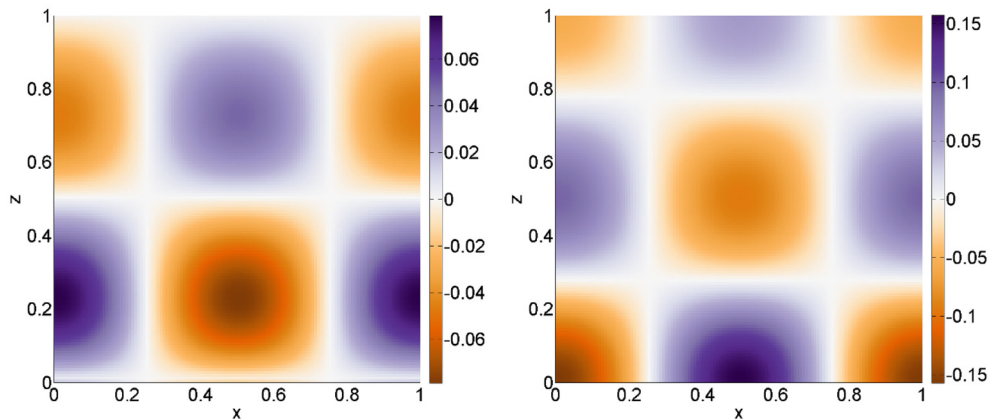

Fig. 8. The numerical solution for two-dimensional waves in a solid wall domain for a stratified incompressible fluid after three periods. The left image shows the vertical velocity field and the right image the pressure field. The number of elements in each direction was 128 and the polynomial order was zero.
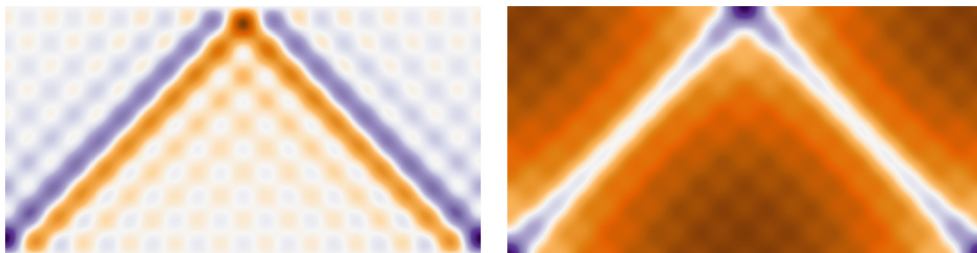

Fig. 9. The numerical solution for the two-dimensional internal gravity waves for the Euler–Boussinesq equations, (69), after three periods. The left image shows the density field and the right image the pressure field. The number of elements in the vertical direction was 128 and the polynomial order was zero.

By superposing ten modes a beam of internal gravity waves is simulated. Table 5 presents the L^2-error and order of convergence of the numerical solution after three periods. The energy and divergence of the velocity field are conserved up to machine precision. Fig. 9 shows the numerical solution after three periods.

Table 5
L^2-error and order of convergence of the numerical solution after three periods for the two-dimensional internal gravity waves for the Euler–Boussinesq equations. The number of elements in the x-direction is twice the number of elements in the z-direction.

$N_p = 0$ $K_x \times K_z$	$\rho_0 u$		$\rho_0 w$		ρ		P	
	L^2-error	Order	L^2-error	Order	L^2-error	Order	L^2-error	Order
8×4	6.70E+0	–	6.09E+0	–	5.12E+0	–	6.28E−1	–
16×8	6.62E+0	0.02	5.99E+0	0.02	6.54E+0	−0.35	3.98E−1	0.66
32×16	3.46E+0	0.93	3.46E+0	0.79	6.93E+0	−0.08	2.31E−1	0.79
64×32	1.88E+0	0.88	1.88E+0	0.88	3.75E+0	0.88	1.03E−1	1.16
128×64	9.57E−1	0.97	9.57E−1	0.97	1.91E+0	0.97	5.12E−2	1.01
256×128	4.81E−1	0.99	4.81E−1	0.99	9.62E−1	0.99	2.61E−2	0.97

$N_p = 1$ $K_x \times K_z$	$\rho_0 u$		$\rho_0 w$		ρ		P	
	L^2-error	Order	L^2-error	Order	L^2-error	Order	L^2-error	Order
8×4	6.96E+0	–	7.10E+0	–	6.12E+0	–	4.45E−1	–
16×8	5.13E+0	0.44	6.59E+0	0.11	7.77E+0	−0.34	2.43E−1	0.87
32×16	2.28E+0	1.17	2.40E+0	1.46	4.59E+0	0.76	9.32E−2	1.38
64×32	9.01E−1	1.34	7.07E−1	1.76	1.44E+0	1.67	3.48E−2	1.42

$N_p = 2$ $K_x \times K_z$	$\rho_0 u$		$\rho_0 w$		ρ		P	
	L^2-error	Order	L^2-error	Order	L^2-error	Order	L^2-error	Order
8×4	5.82E+0	–	5.46E+0	–	1.05E+1	–	2.98E−1	–
16×8	3.27E+0	0.83	3.43E+0	0.67	1.06E+1	−0.01	1.46E−1	1.03
32×16	9.45E−1	1.79	8.08E−1	2.09	1.60E+0	2.72	4.84E−2	1.59
64×32	1.25E−1	2.92	1.26E−1	2.68	2.51E−1	2.68	1.97E−2	1.29

$N_p = 3$ $K_x \times K_z$	$\rho_0 u$		$\rho_0 w$		ρ		P	
	L^2-error	Order	L^2-error	Order	L^2-error	Order	L^2-error	Order
8×4	7.42E+0	–	1.03E+1	–	1.58E+1	–	4.70E−1	–
16×8	5.66E+0	0.39	7.17E+0	0.52	1.28E+1	0.30	2.35E−1	1.00
32×16	1.57E+0	1.85	1.71E+0	2.07	3.46E+0	1.89	3.80E−2	2.63
64×32	1.24E−1	3.66	6.01E−2	4.83	1.23E−1	4.82	1.81E−2	1.07

5.5. Internal gravity waves in non-uniform stratification

We consider continuous profiles of the buoyancy frequency, $N(z)$, and assume that the fluid is stably stratified, $N(z) > 0$. We choose a rectangular domain $\Omega = [0, L] \times [0, 1]$, which is periodic in the horizontal direction and has solid walls in the vertical direction. Suppose that at some depth z_* we find a 'turning point', the depth where internal gravity waves turn from oscillatory behavior, $N(z) > \sigma$, to exponentially decaying behavior, $N(z) < \sigma$. Performing a Taylor expansion around this depth and retaining only the first two terms yields

$$N^2(z) = N_0^2 + \lambda(z - 1), \tag{70}$$

where $N_0^2 = N^2(z_*) - \lambda(z_* - 1)$ is the buoyancy frequency at the surface and $\lambda = N^{2\prime}(z_*)$ is the gradient of the buoyancy frequency. Choosing $N_0^2 = 1$, $\lambda = \frac{1}{2}$ and a frequency $\sigma = \sqrt{\frac{2}{3}}$ yields a turning point at depth $z_* = 1/3$.

A solution to (5), after scaling such that $g = 1$, is found in terms of Airy functions [33]

$$
\begin{aligned}
u &= \frac{k}{k_1}\left(-\mathrm{Ai}'\left[-k(z - \frac{1}{3})\right] + \frac{\mathrm{Ai}\left[-\frac{2}{3}k\right]}{\mathrm{Bi}\left[-\frac{2}{3}k\right]}\mathrm{Bi}'\left[-k(z - \frac{1}{3})\right]\right)\cos(k_1 x - \sqrt{\frac{2}{3}}t), \\[2mm]
w &= \left(\mathrm{Ai}\left[-k(z - \frac{1}{3})\right] - \frac{\mathrm{Ai}(-\frac{2}{3}k)}{\mathrm{Bi}(-\frac{2}{3}k)}\mathrm{Bi}\left[-k(z - \frac{1}{3})\right]\right)\sin(k_1 x - \sqrt{\frac{2}{3}}t), \\[2mm]
\rho &= \sqrt{\frac{3}{2}}N^2(z)\left(\mathrm{Ai}\left[-k(z - \frac{1}{3})\right] - \frac{\mathrm{Ai}(-\frac{2}{3}k)}{\mathrm{Bi}(-\frac{2}{3}k)}\mathrm{Bi}\left[-k(z - \frac{1}{3})\right]\right)\cos(k_1 x - \sqrt{\frac{2}{3}}t), \\[2mm]
P &= \frac{\sqrt{\frac{2}{3}}k}{k_1^2}\left(-\mathrm{Ai}'\left[-k(z - \frac{1}{3})\right] + \frac{\mathrm{Ai}(-\frac{2}{3}k)}{\mathrm{Bi}(-\frac{2}{3}k)}\mathrm{Bi}'\left[-k(z - \frac{1}{3})\right]\right)\cos(k_1 x - \sqrt{\frac{2}{3}}t),
\end{aligned} \tag{71}
$$

where Ai is an Airy function of the first kind, Bi is an Airy function of the second kind, $k = \sqrt[3]{3/4k_1^2}$ and k_1 is the wavenumber of the first mode. The wave numbers are found by applying the boundary conditions in the vertical direction, yielding a dispersion relation

Table 6

L^2-error and order of convergence of the numerical solution after three periods for the two-dimensional internal gravity waves for the Euler–Boussinesq equations in a non-uniform stratification. The number of elements in the x-direction is chosen such that the element dimensions in both directions is approximately equal.

$N_p = 0$ $K_x \times K_z$	$\rho_0 u$		$\rho_0 w$		ρ		P	
	L^2-error	Order	L^2-error	Order	L^2-error	Order	L^2-error	Order
4×4	2.99E−1	–	5.88E−1	–	5.85E−1	–	4.29E−2	–
7×8	1.28E−1	1.22	2.65E−1	1.15	2.66E−1	1.14	1.50E−2	1.51
13×16	5.78E−2	1.15	1.25E−1	1.08	1.24E−1	1.09	6.26E−3	1.26
26×32	2.77E−2	1.06	6.04E−2	1.05	6.01E−2	1.05	2.92E−3	1.10
52×64	1.37E−2	1.02	2.99E−2	1.01	2.98E−2	1.01	1.43E−3	1.03
103×128	6.85E−3	1.00	1.50E−2	1.00	1.49E−2	1.00	7.15E−4	1.00
206×256	3.43E−3	1.00	7.50E−3	1.00	7.46E−3	1.00	4.20E−4	0.91
$N_p = 1$ $K_x \times K_z$	$\rho_0 u$		$\rho_0 w$		ρ		P	
	L^2-error	Order	L^2-error	Order	L^2-error	Order	L^2-error	Order
4×4	1.20E−1	–	3.22E−1	–	3.11E−1	–	1.04E−2	–
7×8	4.22E−2	1.51	1.13E−1	1.51	1.13E−1	1.46	2.77E−2	-1.41
13×16	1.80E−2	1.23	4.77E−2	1.24	4.76E−2	1.25	2.09E−3	3.73
26×32	8.59E−3	1.07	2.24E−2	1.09	2.22E−2	1.10	1.02E−3	1.03
52×64	4.24E−3	1.02	1.10E−2	1.02	1.09E−2	1.03	5.06E−4	1.01
$N_p = 2$ $K_x \times K_z$	$\rho_0 u$		$\rho_0 w$		ρ		P	
	L^2-error	Order	L^2-error	Order	L^2-error	Order	L^2-error	Order
4×4	2.99E−2	–	9.22E−2	–	9.28E−2	–	4.35E−3	–
7×8	5.40E−3	2.47	1.14E−2	3.02	1.15E−2	3.01	3.13E−3	0.47
13×16	7.39E−4	2.87	1.48E−3	2.94	1.55E−3	2.89	2.26E−4	3.79
26×32	9.30E−5	2.99	1.84E−4	3.01	1.93E−4	3.00	5.49E−5	2.04
52×64	1.17E−5	2.99	2.30E−5	3.00	2.41E−5	3.00	1.36E−5	2.01
$N_p = 3$ $K_x \times K_z$	$\rho_0 u$		$\rho_0 w$		ρ		P	
	L^2-error	Order	L^2-error	Order	L^2-error	Order	L^2-error	Order
4×4	3.86E−2	–	1.21E−1	–	1.12E−1	–	2.98E−2	–
8×7	4.13E−3	3.23	1.61E−2	2.90	1.59E−2	2.81	7.89E−4	5.24
13×16	6.35E−4	2.70	2.17E−3	2.89	2.12E−3	2.91	2.67E−5	4.88
26×32	6.74E−5	3.24	2.67E−4	3.02	2.58E−4	3.04	6.40E−6	2.06

$$\mathrm{Ai}\left[\frac{1}{3}k\right]\mathrm{Bi}\left[-\frac{2}{3}k\right] - \mathrm{Bi}\left[\frac{1}{3}k\right]\mathrm{Ai}\left[-\frac{2}{3}k\right] = 0. \tag{72}$$

The wavenumbers are incommensurable: $k_n/k_l \neq n/l$. We cannot fit a beam of internal gravity waves (by adding multiple modes) into a channel of length L which is periodic in the horizontal direction. We choose to use the first mode: the first root of (72) yields the value of the first wavenumber, $k_1 \approx 7.822$. Choosing the length of the domain as $L = 2\pi/k_1 \approx 0.803$ ensures the solution is periodic in the horizontal direction.

Table 6 presents the L^2-error and order of convergence of the numerical solution after three periods. The energy, divergence of the velocity field, mass and momentum in two directions are conserved up to machine precision. Fig. 10 shows the error in total mass during 100 periods.

Fig. 11 shows the numerical solution after three periods. The right image shows the density field. Above the turning depth, $z > 0.33$, the solution shows oscillatory behavior. Looking in the vertical direction, the density field shows half an oscillation in the vertical, with a local extremum at $z = 2/3$. Below the turning depth, $z < 1/3$, the solution is decaying.

5.6. Wave attractors

In the previous test cases, the walls were either parallel or perpendicular to the direction of gravity. Wave attractors appear when there is a geometric asymmetry with respect to the direction of gravity. A slight tilt in one of the walls results in symmetry breaking and hence in wave focusing and defocussing. Focusing dominates and wave attractors appear. Here, as in [4,12] the symmetry is broken by rotating the direction of gravity with respect to the geometry.

Consider (5) in a two-dimensional geometry. When we rotate the direction of gravity by an angle γ, gravity also has a component in the x-direction: $g = g(\sin(\gamma), \cos(\gamma))$. For $\gamma = 0$ the direction of gravity is aligned with the geometry and the symmetry is not broken. No wave attractors can appear. For $\gamma \neq 0$ the direction of gravity is inclined with respect to the geometry and the symmetry is broken. Wave attractors can appear.

The qualitative behavior of the numerical solution is checked. In [12] the free evolution of wave attractors is discussed. The authors use a Hamiltonian finite difference scheme to study wave attractors. We use the same initial condition as in one of the cases discussed in [12]. This initial condition is a $(1, 1)$ Fourier mode in the velocity,

$$u = -\pi \sin(\pi x)\cos(\pi z), \quad w = \pi \cos(\pi x)\sin(\pi z), \quad \rho = 0, \quad P = 0. \tag{73}$$
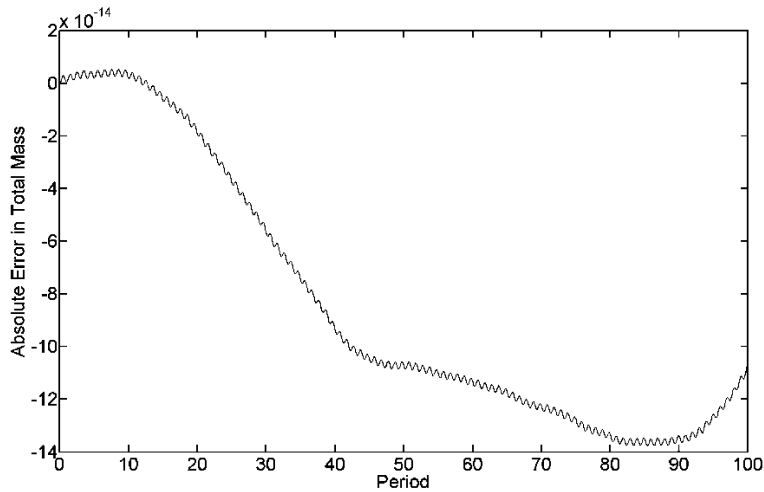
Fig. 10. The absolute error in total mass of the numerical solution for two-dimensional internal gravity waves in a channel with a non-uniform stratification during 100 periods. The number of elements in the horizontal direction was 13, the number of elements in the vertical direction was 16 elements and the polynomial order was zero.
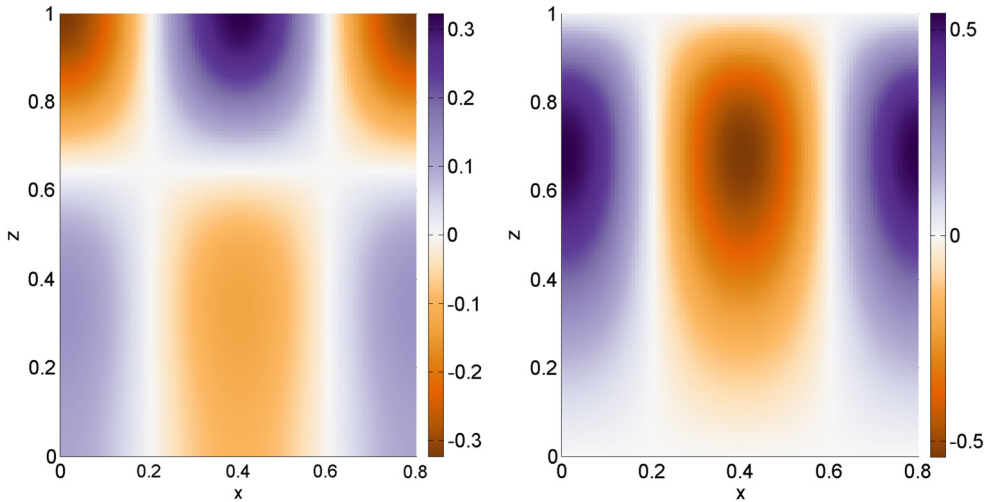

Fig. 11. The numerical solution for the two-dimensional internal gravity waves for the Euler–Boussinesq equations in a channel with a non-uniform stratification after three periods. The left image shows the horizontal velocity field and the right image the density field. The number of elements in the horizontal direction was 103, the number of elements in the vertical direction was 128 elements and the polynomial order was zero.

The initial condition evolved into a set of $(1, 1)$ wave attractors for the case $\gamma \neq 0$. Fig. 12 shows the evolution of the solution. The structure of the solution completely changed due to the asymmetry in the geometry. Since the system is unforced, no frequency is forced onto the system. Waves propagate within a continuous frequency band, resulting in a whole family of $(1, 1)$ wave attractors. For the same parameters ($N^2 = 1$ and $\gamma = \pi/20$) and the same initial conditions the resulting wave attractors are the same as those in [12].

6. Concluding remarks

A DGFEM discretization has been developed for the Hamiltonian dynamics of stratified compressible and incompressible linear ideal fluids. The continuous Poisson bracket and continuous Hamiltonian corresponding to a linear compressible stratified fluid were discretized, yielding a discrete Poisson bracket and discrete Hamiltonian. These discrete objects yielded the discrete equations of motion for compressible stratified fluids. By constructing these discrete equations from a Poisson bracket, the discrete equations possessed a Hamiltonian structure. Together with a symplectic time integration, the modified midpoint rule, this Hamiltonian structure ensured phase space preservation and exact preservation of the discrete energy. This discretization of Hamiltonian dynamics of a compressible fluid was implemented and tested against exact solutions. This provided an intermediate check point for the introduced discretization. Dirac's method of constraints was applied to the discrete Poisson bracket, to enforce the incompressibility of the fluid. Performing a discrete Boussinesq approximation
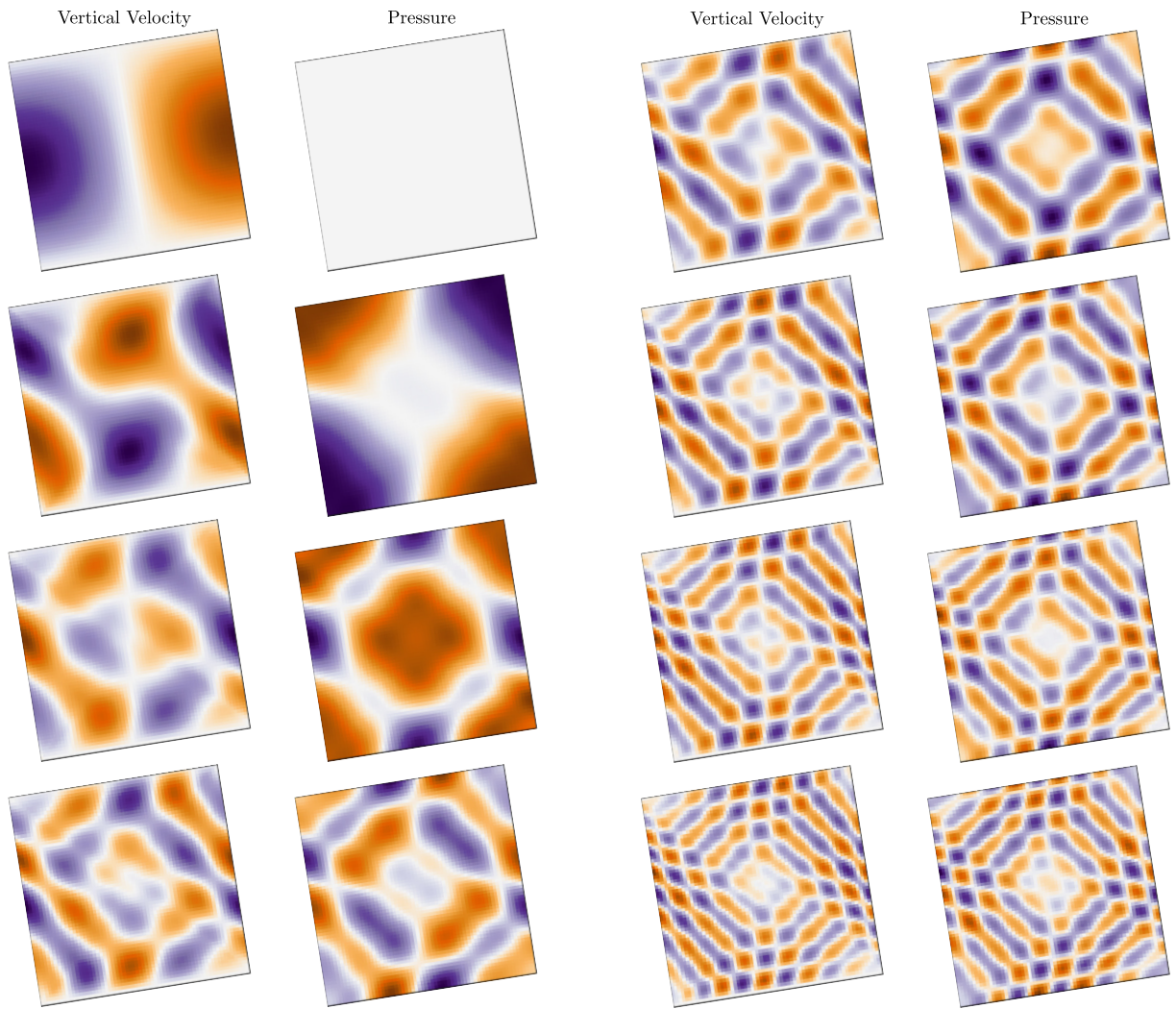
Vertical Velocity   Pressure   Vertical Velocity   Pressure

Fig. 12. The time evolution of the numerical solution for an asymmetric domain relative to the direction of gravity, which points downwards. The evolution goes from the top left to the bottom left and continues from the top right to the bottom right. The left images (first and third columns) shows the vertical velocity and the right images (second and fourth columns) the pressure. The number of elements in each direction was 64 and the polynomial order was two.

preserved the discrete Hamiltonian dynamics and the discrete equations of motion for an Euler–Boussinesq fluid were derived. The construction using Poisson brackets and Dirac's method of constraint ensured the conservation of phase space and the exact conservation of energy and divergence of the velocity field. The developed numerical method is unconditionally stable and does not require a stabilization common to some direct (DG)FEM discretizations of incompressible fluids.

This DGFEM discretization has been verified with analytical solutions. Convergence tables for several tests in stratified fluids were presented. Compressible and incompressible stratified wave solutions in two-dimensional and three-dimensional domains with periodic and solid wall boundary conditions were tested. Global h-refinement and global p-refinement were used and the order of convergence was satisfactory. For all tests the discrete energy was conserved up to machine precision.

By changing the direction of gravity in the model a geometric asymmetry was introduced. Starting from a Fourier mode as initial condition the asymmetry led to a focusing of wave energy and the evolution of wave attractors. Despite the focusing of wave energy, the energy of the system was conserved up to machine precision by construction.

Acknowledgements

References

[1] L.R.M. Maas, F.-P.A. Lam, Geometric focusing of internal waves, J. Fluid Mech. 300 (1995) 1–41.
[2] L.R.M. Maas, D. Benielli, J. Sommeria, F.-P.A. Lam, Observation of an internal wave attractor in a confined, stably stratified fluid, Nature 388 (6642) (1997) 557–561.
[3] N. Grisouard, C. Staquet, I. Pairaud, Numerical simulation of a two-dimensional internal wave attractor, J. Fluid Mech. 614 (2008) 1–14.
[4] G.I. Ogilvie, Wave attractors and the asymptotic dissipation rate of tidal disturbances, J. Fluid Mech. 543 (2005) 19–44.
[5] S. Drijfhout, L.R.M. Maas, Impact of channel geometry and rotation on the trapping of internal tides, J. Phys. Oceanogr. 37 (11) (2007) 2740–2763.
[6] C. Brouzet, I. Sibgatullin, H. Scolan, E. Ermanyuk, T. Dauxois, Internal wave attractors examined using laboratory experiments and 3D numerical simulations, J. Fluid Mech. 793 (2016) 109–131.
[7] V. Lucarini, R. Blender, C. Herbert, F. Ragone, S. Pascale, J. Wouters, Mathematical and physical ideas for climate science, Rev. Geophys. 52 (4) (2014) 809–859.
[8] R.J. LeVeque, Numerical Methods for Conservation Laws, Birkhäuser, 1990.
[9] R. Sadourny, The dynamics of finite-difference models of the shallow-water equations, J. Atmos. Sci. 32 (4) (1975) 680–689.
[10] L.R.M. Maas, Wave attractors: linear yet nonlinear, Int. J. Bifurc. Chaos 15 (09) (2005) 2757–2782.
[11] L.R.M. Maas, Exact analytic self-similar solution of a wave attractor field, Physica D 238 (5) (2009) 502–505.
[12] J. Bajars, J. Frank, L.R.M. Maas, On the appearance of internal wave attractors due to an initial or parametrically excited disturbance, J. Fluid Mech. 714 (2013) 283–311.
[13] S. Nurijanyan, J.J.W. Van Der Vegt, O. Bokhove, Hamiltonian discontinuous Galerkin FEM for linear, rotating incompressible Euler equations: inertial waves, J. Comput. Phys. 241 (2013) 502–525.
[14] Y. Xu, J.J.W. Van Der Vegt, O. Bokhove, Discontinuous Hamiltonian finite element method for linear hyperbolic systems, J. Sci. Comput. 35 (2–3) (2008) 241–265.
[15] R. Salmon, Semigeostrophic theory as a Dirac-bracket projection, J. Fluid Mech. 196 (1988) 345–358.
[16] J. Vanneste, O. Bokhove, Dirac-bracket approach to nearly geostrophic Hamiltonian balanced models, Physica D 164 (3) (2002) 152–167.
[17] O. Bokhove, Balanced models in geophysical fluid dynamics: Hamiltonian formulation, constraints and formal stability, in: Large-Scale Atmosphere–Ocean Dynamics II, 2002, pp. 1–63.
[18] S. Balay, S. Abhyankar, M.F. Adams, J. Brown, P. Brune, K. Buschelman, L. Dalcin, V. Eijkhout, W.D. Gropp, D. Kaushik, M.G. Knepley, L.C. McInnes, K. Rupp, B.F. Smith, S. Zampini, H. Zhang, PETSc Web page, http://www.mcs.anl.gov/petsc, 2016.
[19] S. Balay, S. Abhyankar, M.F. Adams, J. Brown, P. Brune, K. Buschelman, L. Dalcin, V. Eijkhout, W.D. Gropp, D. Kaushik, M.G. Knepley, L.C. McInnes, K. Rupp, B.F. Smith, S. Zampini, H. Zhang, H. Zhang, PETSc users manual, Tech. Rep. ANL-95/11 – Revision 3.7, Argonne National Laboratory, 2016.
[20] L. Pesch, A. Bell, H. Sollie, V.R. Ambati, O. Bokhove, J.J.W. Van Der, Vegt, hpGEM—a software framework for discontinuous Galerkin finite element methods, ACM Trans. Math. Softw. 33 (4) (2007) 23.
[21] R. Salmon, Hamiltonian fluid mechanics, Annu. Rev. Fluid Mech. 20 (1) (1988) 225–256.
[22] P.J. Morrison, Hamiltonian description of the ideal fluid, Rev. Mod. Phys. 70 (2) (1998) 467.
[23] M.E. McIntyre, T.G. Shepherd, An exact local conservation theorem for finite-amplitude disturbances to non-parallel shear flows, with remarks on Hamiltonian structure and on Arnol'd's stability theorems, J. Fluid Mech. 181 (1987) 527–565.
[24] P.J. Morrison, J.M. Greene, Noncanonical Hamiltonian density formulation of hydrodynamics and ideal magnetohydrodynamics, Phys. Rev. Lett. 45 (10) (1980) 790.
[25] P.J. Morrison, Poisson brackets for fluids and plasmas, in: Mathematical Methods in Hydrodynamics and Integrability in Dynamical Systems, vol. 88, 1982, pp. 13–46.
[26] T.G. Shepherd, Symmetries, conservation laws, and Hamiltonian structure in geophysical fluid dynamics, Adv. Geophys. 32 (287–338) (1990) 2.
[27] T.G. Shepherd, A unified theory of available potential energy 1, Atmos.-Ocean 31 (1) (1993) 1–26.
[28] D.G. Andrews, A note on potential energy density in a stratified compressible fluid, J. Fluid Mech. 107 (1) (1981) 227–236.
[29] P.A.M. Dirac, Generalized Hamiltonian dynamics, Proc. Phys. Soc. Lond., Sect. A. Math. Phys. Sci. 246 (1246) (1958) 326–332.
[30] P.A. Dirac, Lectures on Quantum Mechanics, Courier Corporation, 2013.
[31] E. Hairer, C. Lubich, G. Wanner, Geometric Numerical Integration: Structure-Preserving Algorithms for Ordinary Differential Equations, vol. 31, Springer, 2006.
[32] A.M. van Oers, Hamiltonian discontinuous Galerkin finite element method for internal gravity waves: an energy and structure conserving discretization, Master's thesis, TU Delft, Delft University of Technology, 2015.
[33] T. Gerkema, J.T.F. Zimmerman, An Introduction to Internal Waves, Royal NIOZ, 2008.